DIURNAL EVOLUTION OF THE OXYGEN ISOTOPE ANOMALY OF CO$_2$ ABOVE A FOREST ECOSYSTEM

by

Evelyn Workman

6496660

A thesis submitted for the degree of Master of Science

at

UTRECHT UNIVERSITY

INSTITUTE OF MARINE AND ATMOSPHERIC RESEARCH

Universiteit Utrecht

July 2020

Abstract

The oxygen isotope anomaly (Δ^{17}O) of atmospheric CO_2 has been proposed as a better tracer of the gross CO_2 fluxes between the atmosphere and the biosphere than the δ^{18}O signal, due to physiochemical processes in the biosphere following mass dependent isotope fractionation. In the first part of this thesis, we prepared and characterised an automated system to measure the oxygen isotope anomaly (Δ^{17}O) of atmospheric CO_2. The fractionation factors of the CO_2-O_2 isotope exchange reaction are determined at different reaction temperatures experimentally, and the results confirm that the fractionation factor has a temperature dependence. There is an offset between the fractionation factors found experimentally in this study and fractionation factors which are calculated theoretically. The reason for this offset is still unknown, however it could be due to real gas effects compared to ideal gas effects, or due to inconsistencies between the isotopic scales. In the second part of this thesis, a mixed layer model simulating a convective atmospheric boundary layer above a forest ecosystem is used to simulate the diurnal evolution of the Δ^{17}O signature of atmospheric CO_2. The model is used to investigate the relative contributions from entrainment, soil and plant to the temporal budget of Δ^{17}O of atmospheric CO_2 under different meteorological conditions, and we find that the contribution from the plant is the most sensitive to changes in the meteorology (specifically, humidity), indicating the temporal budget is dependent on photosynthesis activity.

Contents

Introduction

Atmospheric CO_2 has several sources and sinks, which are shown in the carbon cycle diagram, Figure 1.1 (adapted from Joiner et al. (2018)). Figure 1.1 shows that the main CO_2 sinks are the biosphere and the ocean, and the main CO_2 sources are from fossil fuel burning and land use change. The overall effect is that the concentration of CO_2 in the atmosphere is rising at a rate of 4.7 PgC/yr (Joiner et al. 2018). The biospheric sink consists of two large CO_2 fluxes, the total respiration flux, which adds CO_2 to the atmosphere, and the gross photosynthesis flux (gross primary productivity, GPP), which removes CO_2 from the atmosphere. The biosphere is a net CO_2 sink as the photosynthesis flux is slightly larger than the respiration flux. The relatively small difference between the total respiration and photosynthesis fluxes is is equal to 3.2 ± 0.7 PgC/yr (Joiner et al. 2018). This small imbalance is significant when compared to the amount of CO_2 released from the burning of fossil fuels, 9.4 PgC/yr (Joiner et al. 2018) (see Figure 1.1). Estimates of the respiration and photosynthesis fluxes are subject to large uncertainties, for example estimates of the gross photosynthesis flux are currently poorly constrained, ranging between 116-175 PgC/yr (Joiner et al. 2018). As atmospheric CO_2 concentrations continue to rise, it is important that the total amount of CO_2 removed from the atmosphere by the biosphere is more precisely known, and that we understand how this sink will evolve in the future under these increased atmospheric CO_2 concentration and higher temperature scenarios. This means the gross photosynthesis and respiration fluxes need to be better quantified, one approach to this is analysing the isotopic composition of atmospheric CO_2.

The three most abundant oxygen isotopologues of atmospheric CO_2 are $C^{16}O^{16}O$, $C^{17}O^{16}O$ and $C^{18}O^{16}O$, with relative abundances of 99.5%, 0.077%, and 0.041%, respectively (Eiler & Schauble 2004). Investigating the $\delta^{18}O$ signal of tropospheric CO_2 (the ratio of ^{18}O to ^{16}O in CO_2) can help improve understanding of the bisopheric component of the CO_2 budget, as the $\delta^{18}O$ signal of tropospheric CO_2 is largely determined by the activity of the biosphere; photosynthesis and respiration have two distinct $\delta^{18}O$ of CO_2 ($\delta^{18}O(CO_2)$) signals (Farquhar et al. 1993, Ciais et al. 1997). Most of the CO_2 that enters the leaf via the stomata will exchange isotopes with the leaf water (which is more enriched in ^{18}O than
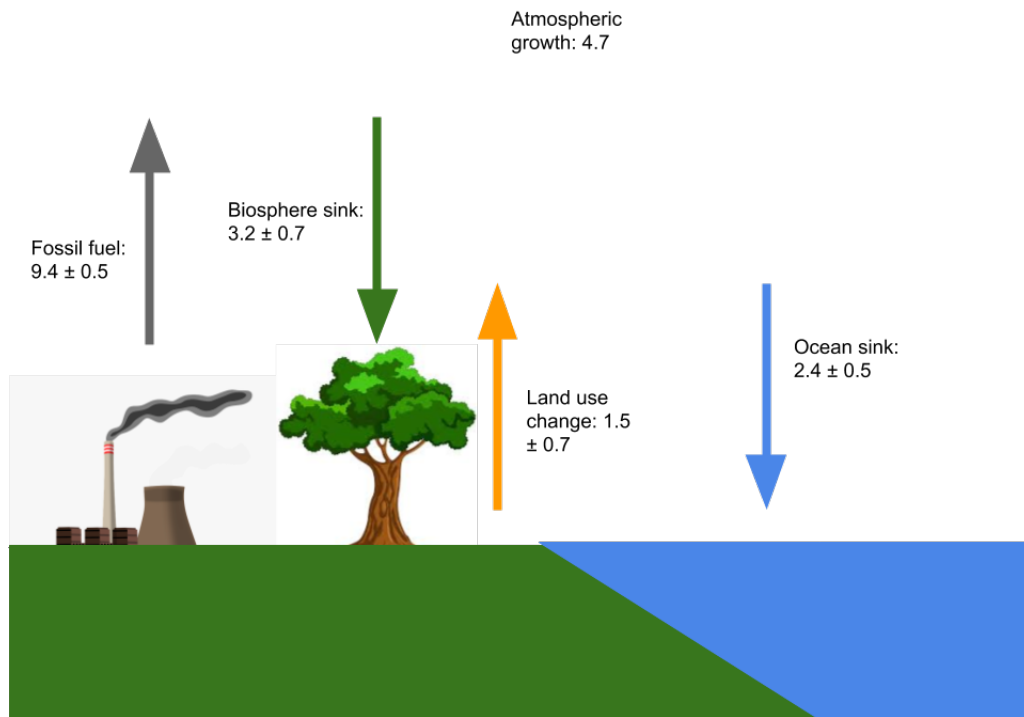
Figure 1.1: Simplified schematic of the global carbon cycle averaged globally for 2008-2017, adapted from Joiner et al. (2018). The arrows represent the annual carbon exchange fluxes, in PgC/year. The grey arrow indicates the CO_2 emissions from buring of fossil fuels, the green arrow indicates the CO_2 flux to the biospheric sink (NEE), the orange arrow indicates emissions due to deforestation and land use change, and the blue arrow indicates the uptake of CO_2 by the ocean sink. The uncertainty on the CO_2 atmospheric growth is 0.02PgC/year.

atmospheric CO_2), thereby obtaining an isotopic composition that is in isotopic equilibrium with the isotopic composition of the leaf water. This CO_2 is back diffused into the atmosphere, increasing the $\delta^{18}O$ value of atmospheric CO_2 (Francey & Tans 1987). Therefore, this back-diffused CO_2 determines the effect of photosynthesis on the $\delta^{18}O(CO_2)$ signature in the atmosphere, and measurements of this signal can help to constrain estimates of GPP. The theory behind the $\delta^{18}O(CO_2)$ signal in the atmosphere is explained in more detail in section 2.

In order to use $\delta^{18}O(CO_2)$ as a tracer for GPP, it is necessary to make estimates of $\delta^{18}O$ values for various water reservoirs, e.g. leaf and soil water. However, the $\delta^{18}O$ signals of these reservoirs can have a strong dependence on many other external factors, therefore making accurate estimates difficult to obtain. For example, an important water reservoir in the $\delta^{18}O(CO_2)$ tropospheric budget is the leaf water reservoir; the $\delta^{18}O$ value of leaf water depends on other external factors, such as the $\delta^{18}O$ distribution in soils, humidity, precipitation and temperature (Hoag et al. 2005). Hoag et al. (2005) proposed that the oxygen isotope anomaly ($\Delta^{17}O$) of tropospheric CO_2 can be used instead of the $\delta^{18}O(CO_2)$ signal to constrain GPP. The $\Delta^{17}O(CO_2)$ atmospheric signal depends much less on the isotopic composition of the water reservoirs compared to $\delta^{18}O$, it is only dependent on the relative difference between the $\delta^{18}O$ and $\delta^{17}O$ values. Therefore, we do not need precise measurements, estimates nor detailed modelling of the $\delta^{18}O$ signal of tropospheric water reservoirs to infer the $\Delta^{17}O(CO_2)$ signal in the troposphere. Several studies modelling the $\Delta^{17}O(CO_2)$ of the troposphere have been developed, including Hoag et al. (2005), Hofmann et al. (2017), Koren et al. (2019).

The initial aim of this thesis is to characterise an automated $\Delta^{17}O$ measurement system in order to prepare it to measure $\Delta^{17}O(CO_2)$ of atmospheric samples from different types of ecosystems. We carry out several experiments to help characterise the system, including investigating the precision and stability of the isotope ratio mass spectrometer (IRMS), and investigating properties of the isotope equilibration reaction between CO_2 and O_2, for example, how the equilibrium reaction time depends on the reaction temperature, and how the fractionation factors for the CO_2-O_2 isotope exchange reaction vary at different temperatures. The characterisation of the system is described in section 3.2. After the characterisation of the system, the system was ready to measure samples of atmospheric CO_2, however the laboratory was closed due to COVID-19, so the scope of this thesis had to be changed.

Therefore, in the second part of this thesis, a coupled land-atmosphere model (Vilà-Guerau de Arellano & van Heerwaarden 2015) is used to simulate the diurnal evolution of $\Delta^{17}O(CO_2)$ in the atmospheric boundary layer (ABL). The $\Delta^{17}O(CO_2)$ signal has been implemented in the model by Koren (2020). In this study, the model is used to investigate

the diurnal evolution of $\Delta^{17}O$ of CO_2 in the ABL, and how local and non-local processes contribute to the diurnal temporal budget of ABL $\Delta^{17}O(CO_2)$. Several sensitivity analyses are carried out to study how sensitive the modelled signal of $\Delta^{17}O(CO_2)$ is to changes in different meteorological conditions.

Theory

2.1 Isotope Theory

The abundance of a particular isotope is often measured as a "double relative". First, it is measured as a ratio relative to the more abundant lighter isotope, e.g. oxygen 18 is measured against oxygen 16, $^{18}\text{R} = \frac{[^{18}\text{O}]}{[^{16}\text{O}]}$. Second, these ratios are measured relative to a reference material (in this study we use VSMOW), which is represented by the δ value,

$$\delta^{18} = \left(\frac{^{18}\text{R}_{sample}}{^{18}\text{R}_{standard}} - 1 \right) \tag{2.1}$$

These δ values are very small and are expressed in per mil (‰). If the sample is enriched in the heavy isotope relative to the standard, then the δ value will be positive, and when it is depleted in the heavy isotope relative to the standard, the δ value will be negative. Processes such as diffusion and evaporation can change the isotopic composition of oxygen containing molecules; as these processes are dependent on the mass of the molecules, the resulting fractionation is referred to as mass-dependent fractionation. Mass-dependent fractionation means that the fractionation in ^{18}O is approximately twice as large as that in ^{17}O, as the mass difference between ^{16}O and ^{18}O is twice as large as the mass difference between ^{16}O and ^{17}O.

The isotope anomaly (or 17O-excess) is the deviation of a fractionation process from mass-dependent fractionation. It is defined by the equation,

$$\Delta^{17}\text{O} = \ln(\delta^{17}\text{O} + 1) - \lambda_{RL}\ln(\delta^{18}\text{O} + 1), \tag{2.2}$$

where λ_{RL} is the reference line for mass-dependent fractionation. Different values of λ_{RL} are used in literature, ranging from 0.5 to 0.53 (Hofmann et al. 2017), this is because the definition of mass-dependent fractionation varies according to the process which is being considered. In this study we will use the reference line associated with the isotopic composition of precipitation (meteoric water), $\lambda_{RL} = 0.528$ (Meijer & Li 1998), as this is
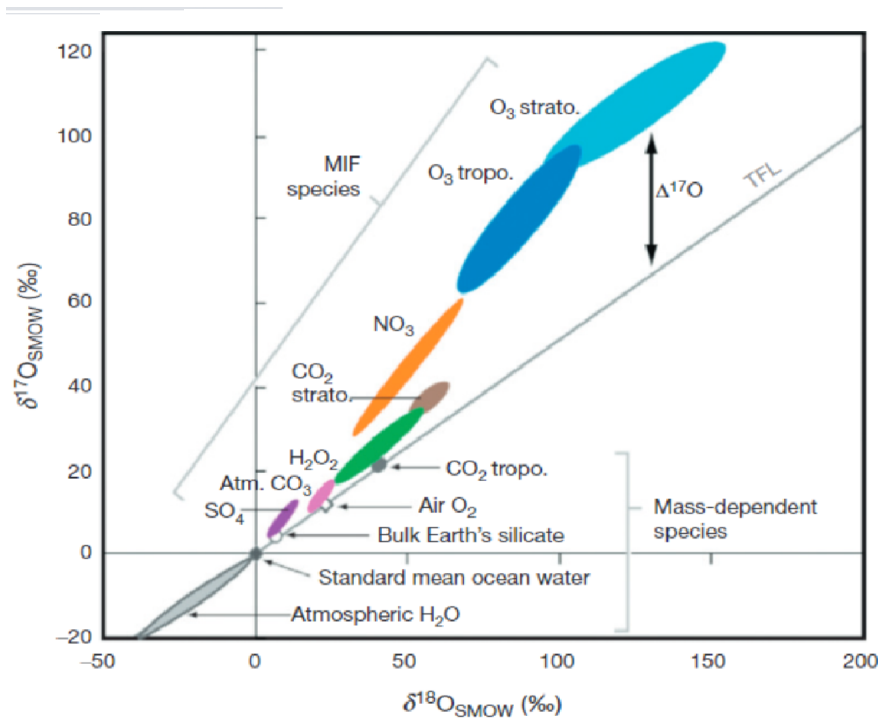
7

Figure 2.1: Three-isotope plot for oxygen in a terrestrial environment (Thiemens 2006). In this graph, the linear definition of $\Delta^{17}O$ is used (equation 2.3) and $\delta^{17}O$ vs $\delta^{18}O$ is plotted. Mass-dependent species and mass-independent fractionation (MIF) species are highlighted on the figure.

a key process in the determination of the $\Delta^{17}O$ value in tropospheric CO_2. If the δ values are sufficiently small, then we can assume a linear definition of $\Delta^{17}O$,

$$\Delta^{17}O = \delta^{17}O - \lambda_{RL}\ln\delta^{18}O. \tag{2.3}$$

As this linear definition is only valid at small δ values, the error on the linear definition of $\Delta^{17}O$ will increase as the δ values increase.

Figure 2.1 shows the three-isotope plot for oxygen 17 and oxygen 18. The terrestrial fractionation line (TFL) is the line which represents mass-dependent fractionation, with a slope equal to λ_{RL} (in the case of Figure 2.1 $\lambda_{RL} = 0.52$). Species which lie on the line are mass-dependent species, $\delta^{17}O \approx \lambda_{RL}\delta^{18}O$ (using the linear definition of $\Delta^{17}O$, equation 2.3). The species that lie off the reference line are mass-independent species ($\Delta^{17}O \neq 0$), although small positive and negative $\Delta^{17}O$ occur from purely mass dependent processes due to the different three isotope slopes associated with different processes. $\Delta^{17}O$ is represented by how far the species deviates from the TFL on the plot (see Figure 2.1). An example of a mass-independent fractionation process is the formation of ozone in the stratosphere, this is described in more detail in section 2.2.

2.2 The Δ^{17}O Signal in the Stratosphere, Troposphere and Biosphere

Stratospheric (and tropospheric) ozone is enriched in heavy isotopes (Yung et al. 1991). When this ozone undergoes photolysis, electronically excited $O(^1D)$ atoms can isotopically exchange with CO_2 and transfer its heavy isotopes to CO_2. The photolysis reaction sequence which produces CO_2 is described in the reaction equations below,

$$O_3 + h\nu \longrightarrow O_2 + O(^1D)$$

$$CO_2 + O(^1D) \longrightarrow CO_3^*$$

$$CO_3^* \longrightarrow CO_2 + O(^3P)$$
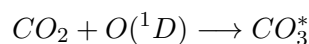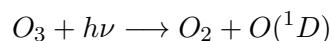
Stratospheric ozone will have a mass-independent signature ($\Delta^{17}O \gg 0$), as its formation involves a mass-independent process. The resulting stratospheric CO_2 from the photolysis reaction sequence will therefore also have a positive oxygen isotope anomaly ($\Delta^{17}O \gg 0$). The positive $\Delta^{17}O(CO_2)$ signal in the stratosphere leads to a positive $\Delta^{17}O(CO_2)$ signal in the troposphere due to an influx of stratospheric CO_2 into the troposphere.

There are several "sinks" for the positive tropospheric $\Delta^{17}O(CO_2)$ signal, which involve reducing the positive $\Delta^{17}O(CO_2)$ signal in the troposphere. These sinks are water reservoirs which work to reduce the $\Delta^{17}O$ signal of CO_2 by exchanging oxygen isotopes with the CO_2, the CO_2 then obtains an isotopic signature which is in isotopic equilibrium the water. Atmospheric CO_2 isotopically equilibrates with water by the following reaction,

$$CO_2 + H_2^{18}O \Longleftrightarrow CO^{18}O + H_2O \tag{2.4}$$
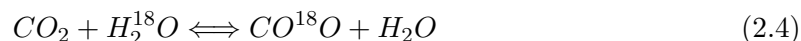
The most important water reservoir for $\Delta^{17}O(CO_2)$ is leaf water (Francey & Tans 1987). The isotopic exchange between CO_2 and H_2O takes place much faster in leaves than in other water reservoirs due to the presence of the enzyme carbonic anhydrase (CA), which speeds up reaction (2.4) (Francey & Tans 1987). Of the CO_2 which diffuses into a leaf's stomata, about one third is used in photosynthesis, the remaining two thirds diffuses back out into the atmosphere after undergoing isotopic exchange with the chloroplast water (Cuntz 2003). Chloroplast water is enriched in ^{18}O relative to soil water, due to evaporation from the leaf which causes water containing lighter isotopes to be preferentially evaporated over water containing heavier isotopes. This is an example of mass-dependent fractionation. The incoming CO_2 will equilibrate with the chloroplast water resulting in the back-diffused CO_2 being enriched in ^{18}O, relative to tropospheric CO_2 (see reaction 2.4). Due to the large

9

volume of water relative to the volume of atmospheric CO_2 interacting with the water, the isotopic composition of the CO_2 will be influenced by the isotopic composition of the water, while the isotopic composition of the water will be hardly affected by the CO_2. As leaf water is mass-dependently fractionated, the back-diffused CO_2 will have a $\Delta^{17}O(CO_2)$ signal which has a smaller magnitude ($\Delta^{17}O(CO_2) \approx 0$ ‰) compared to the $\Delta^{17}O$ signal of the CO_2 entering the chloroplasts. Therefore, this process of equilibrating CO_2 with leaf water works to decrease the $\Delta^{17}O(CO_2)$ signal of the troposphere.

Soil water is another sink of tropospheric $\Delta^{17}O(CO_2)$. CO_2 released from soils is due to respiration or soil invasion. During soil invasion, CO_2 diffuses into the soil, equilibrates with the soil water, and diffuses back out into the atmosphere (Tans 1998). Soils can also contain CA, and its presence accelerates soil hydration, causing a larger invasion flux from the soil, which carries the isotopic composition of the soil water (Wingate et al. 2009). However, diffusion of CO_2 out of the soil occurs faster than uncatalysed hydration (Kapiluto et al. 2007, Miller et al. 1999), therefore, in soils with low CA concentrations, CO_2 exits the soil largely via molecular diffusion, without having exchanged isotopes with the soil water. The same is true for respired CO_2 from soils, the respired CO_2 exits the soil mainly by diffusion, when CA abundance is limited, before equilibration with soil water can occur.

Part I: Measurement of $\Delta^{17}O(CO_2)$ using an Automated System

3.1 Motivation

The $\Delta^{17}O$ of CO_2 is determined by measuring its $\delta^{17}O$ and $\delta^{18}O$ values. The value of $\delta^{18}O$ can be measured directly on an isotope ratio mass spectrometer (IRMS), however, the value of $\delta^{17}O$ cannot be accurately measured using an IRMS as the isotopologue $^{12}C^{16}O^{17}O$ has almost the same mass as $^{13}C^{16}O^{16}O$. The difference in mass between these two isotopologues is smaller than the resolving power of most mass spectrometer systems. In an IRMS, ionised molecules are separated in a magnetic field based on their different mass-to-charge (m/z) ratios, the magnetic field causes the path of the ionised molecules to curve. Isotopically lighter molecules (e.g. $^{12}C^{16}O^{16}O$, m/z = 44 or $^{16}O^{16}O$, m/z = 32) have a shorter radius of curvature, so will bend more, than isotopically heavier molecules (e.g. $^{12}C^{16}O^{18}O$, m/z = 46 or $^{16}O^{18}O$, m/z = 34). Each beam is focused onto a separate Faraday cup which measures the current generated by the beam. The current measured by each cup is normalised against the current generated by a reference gas, and the delta values can be calculated. Therefore, another method to measure the $\delta^{17}O$ of CO_2 is required.

3.2 Methods

A precise measurement technique has been developed by various groups, e.g. Mahata et al. (2013), Barkan et al. (2015) and Adnew et al. (2019), to measure $\delta^{17}O$ of CO_2, by isotopic equilibration of O_2, with known isotopic composition, with the CO_2 under investigation. The method used to measure the $\Delta^{17}O$ signal of CO_2 in this study follows closely the procedure described by Adnew et al. (2019), with the difference being that the system (apart from the reactor) is made of electropolished stainless steel, and the system is automated starting from cryogenic separation of CO_2 from the air sample through to the measurement

of the oxygen isotope composition equilibrated with CO_2.

Reacting O_2 and CO_2 together allows the molecules to exchange isotopes, and they will eventually reach an isotopic equilibrium, provided the reaction time is long enough. After equilibrium has been reached, the change in the isotopic composition of the O_2 can be measured using an IRMS, which can be used to calculate the initial value of $\delta^{17}O$ of CO_2. This calculation is based on the following mass balance equation for the CO_2-O_2 exchange reaction, which states that the total number of ^{17}O and ^{18}O molecules in the initial CO_2 and O_2 and the final CO_2 and O_2 are the same,

$$m_{O_2}\delta^{17}O_i(O_2) + m_{CO_2}\delta^{17}O_i(CO_2) = m_{O_2}\delta^{17}O_f(O_2) + m_{CO_2}\delta^{17}O_f(CO_2), \qquad (3.1)$$

where m is the number of moles of O_2 or CO_2, the i indices represent the initial isotopic composition before exchange and the f indices represent the final isotopic composition after exchange.

Rearranging equation 3.1 leads to,

$$\delta^{17}O_i(CO_2) = \delta^{17}O_f(CO_2) + \frac{\delta^{17}O_f(O_2) - \delta^{17}O_i(O_2)}{\beta}, \qquad (3.2)$$

where $\beta = \frac{m_{CO_2}}{m_{O_2}}$. However, $\delta^{17}O_f(CO_2)$ is unknown, so we introduce a term called the fractionation factor, $^*\alpha = \frac{\delta^*O(CO_2)+1}{\delta^*O(O_2)+1}$, which is the ratio between the isotopic composition of CO_2 and O_2 after equilibrium has been reached. Including α, equation 3.2 becomes,

$$\delta^{17}O_i(CO_2) = \frac{1}{\beta}\left((\delta^{17}O_f(O_2) + 1)(^{17}\alpha\beta + 1) - (\delta^{17}O_i(O_2) + 1)\right) - 1. \qquad (3.3)$$

The fractionation factors, $^{17}\alpha$ and $^{18}\alpha$, are properties of the CO_2-O_2 exchange reaction. The values for $^{17}\alpha$ and $^{18}\alpha$ can be determined experimentally by isotopically exchanging CO_2 and O_2 of known isotopic composition, and the $\delta^{17}O$ and $\delta^{18}O$ values of the CO_2 and O_2 after equilibrium has been reached can be found, α is then calculated using the definition $^*\alpha = \frac{\delta^*O(CO_2)+1}{\delta^*O(O_2)+1}$.

Due to thermodynamic properties, CO_2 and O_2 won't reach exactly the same isotopic composition, there will be a small difference between the final isotopic values after the equilibrium reaction has been completed. This difference is quantified by the fractionation factor, α. When $\alpha = 1$, the final isotopic composition of CO_2 and O_2 are equal, when $\alpha > 1$, the final isotopic composition of CO_2 is greater than that of O_2, and when $\alpha < 1$, the final isotopic composition of CO_2 is less than that of O_2. A schematic depicting the CO_2-O_2 exchange reaction and α is shown in Figure 3.1. The figure shows that isotopic equilibrium between CO_2 and O_2 is only reached after a certain reaction time.
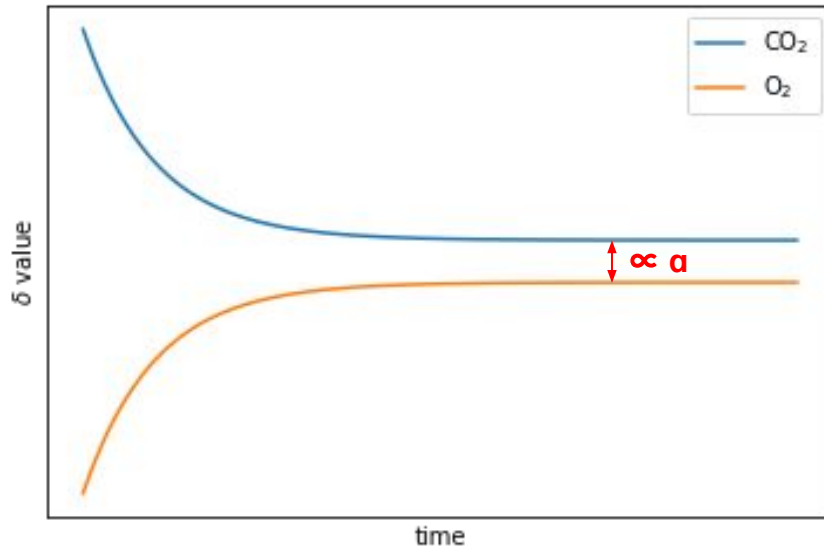
Figure 3.1: A schematic graph depicting an isotopic exchange reaction between CO_2 and O_2. The blue and orange curves represent the isotopic composition of two substances (e.g. CO_2 and O_2) during their reaction, with the x-axis representing the reaction time. The fractionation factor, α is proportional to the difference between the delta values of the two substances when a stable isotopic composition is reached.

Next, the experimental procedure from extraction of the CO_2 from the sample to the CO_2-O_2 isotope exchange reaction to measurement of the isotopic composition of O_2 which has undergone isotopic exchange with the CO_2 on an IRMS.

3.2.1   Experimental Procedure

An schematic of the experimental setup, with the different stages (CO_2 extraction from the the air sample, CO_2-O_2 isotope exchange reaction, CO_2-O_2 separation, and measurement of the O_2 using an isotope ratio mass spectrometer (IRMS)) is shown in Figure 3.2.

The initial δ values of O_2 are $\delta^{17}O(O_2)_i = 7.007 \pm 0.006$ ‰ and $\delta^{18}O(O_2)_i = 14.095 \pm 0.012$ ‰ (errors are standard error of the mean times the student t-test for 95% confidence), these are calculated from the O_2 which is directly introduced into the dual inlet system in section 3.3.1.2 (the average of the teal data points in figures 3.4a and 3.4b). The initial δ values of CO_2 are $\delta^{17}O(CO_2)_i =17.904$ ‰ and $\delta^{18}O(CO_2)_i = 34.655$ ‰.

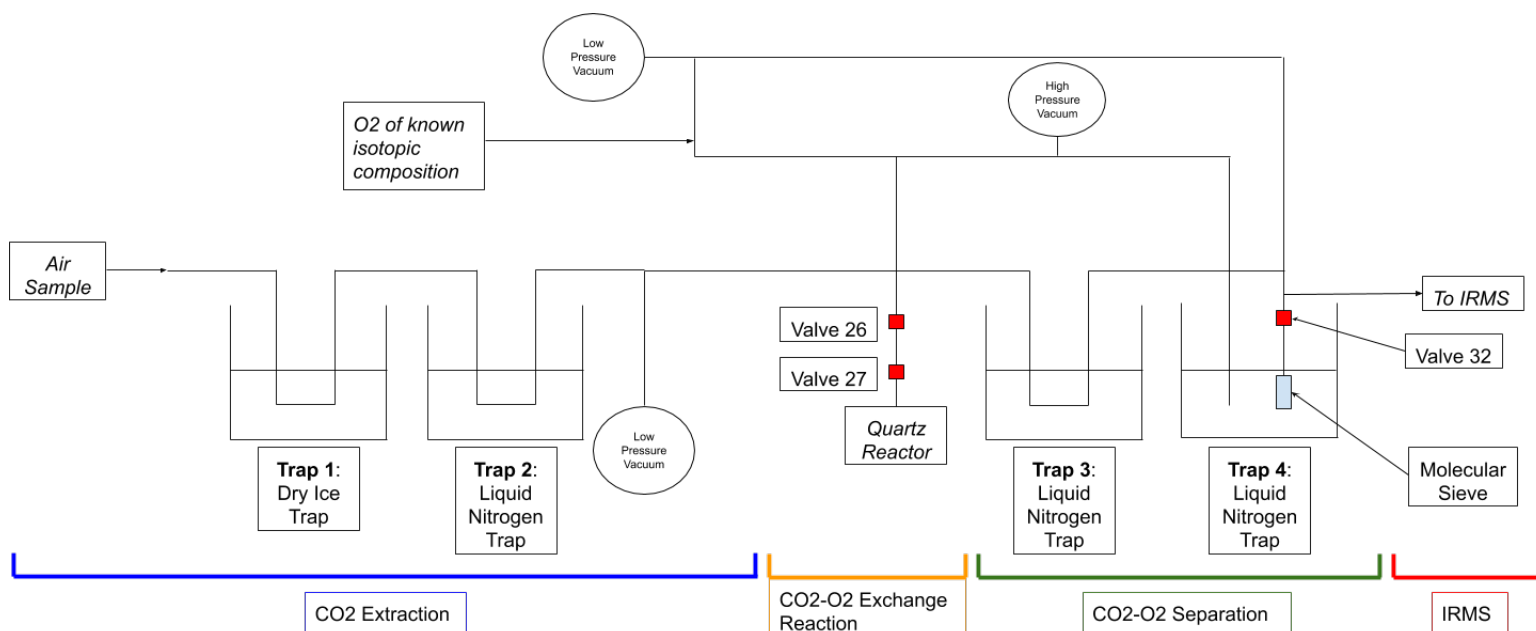Figure 3.2: Schematic of experimental setup. The air sample is introduced into "trap 1" on the left hand side. The CO_2 is cryogenically extracted from the air sample using a dry ice trap and a liquid nitrogen trap in the section labelled "CO_2 extraction". The extracted CO_2 then undergoes isotopic exchange with O_2 of a known isotopic composition, in the section "CO_2-O_2 exchange reaction". The CO_2 and O_2 are separated cryogenically using liquid nitrogen traps in the "CO_2-O_2 separation" section. The isotopic composition of the O_2 is measured in the isotope ratio mass spectrometer (IRMS) in the section "IRMS". Three valves are highlighted in the diagram, valve 26, 27 and 32, as these are referred to later in the text when explaining the CO_2-O_2 isotope exchange. The experimental procedure is described in the text.

3.2.1.1 Extraction of CO_2

CO_2 is first extracted from the sample of air by passing the sample first through two dewar cooling traps, the first traps contains dry ice and the second contains liquid nitrogen (traps 1 and 2, respectively, in Figure 3.2). The first step freezes the water out of the sample, and the second step freezes out CO_2, allowing the remaining gas in the sample to pass through to a low pressure vacuum. After 10 minutes of passing the gas through the dry ice and liquid nitrogen traps, all the CO_2 should be isolated in the liquid nitrogen dewar cooling trap 2. Trap 2 is then lowered, allowing the CO_2 to pass through to the next part of the experiment, where it will be reacted with O_2.

3.2.1.2 CO_2-O_2 Exchange Reaction

The extracted CO_2 is transferred to the quartz reactor. It is trapped in a vertical tube in the quartz reactor cryogenically, using a liquid nitrogen microdosing system (Norhof 900 series LN2 cooling system, Ede, The Netherlands), which continuously adds liquid nitrogen into

the quartz reactor. After the CO_2 has been introduced and trapped in the quartz reactor, an equal quantity of O_2 of known isotopic composition is introduced into the quartz reactor. The O_2 gas entered the system at the point "O_2 of a known isotopic composition" indicated in Figure 3.2. Meanwhile, valve 26 is open and valve 27 is closed (the valves are depicted in Figure 3.2). The gas fills the parts of the system it is open to, so it will enter the steel tube up to valve 27. The gas continues to enter the system until the pressure reads approximately 300 torr on the pressure sensor, and then we close the valve connecting the O_2 cylinder to the system, so no more gas can enter. Valve 26 is then closed. The gas in the rest of the system is removed by a vacuum pump, so we have isolated a particular amount of O_2 gas between valves 27 and 26. This process is referred to as "expanding" the gas between valve 26 and valve 27. The "expanding" process enables us to control the amount of gas we want to measure. The O_2 gas which has been expanded between valve 26 and 27 is then introduced into the quartz reactor and the liquid nitrogen microdosing system is turned off. The CO_2 and O_2 gases are now both contained in the quartz reactor and they can react and exchange isotopes. The reactor contains a platinum catalyst which speeds up the isotope exchange reaction. The reaction occurs for 2 hours at a temperature of 750 °C (Barkan et al. 2015), allowing the CO_2 and O_2 to come to isotopic equilibrium. The quartz reactor containing the platinum catalyst is indicated in Figure 3.2, below valve 27.

3.2.1.3   Separation of CO_2 and O_2

After the exchange, the sample is passed through a liquid nitrogen dewar cooling trap (trap 3 in Figure 3.2) which cryogenically traps the CO_2 in the U trap, and lets the O_2 pass by. The O_2 then enters another liquid nitrogen dewar cooling trap (trap 4 in Figure 3.2) which contains 3 molecular sieve (MS) pellets 5Å, the function of the MS is to adsorb the O_2 onto its pores. The pores of the MS pellets chosen are large enough to catch the O_2 molecules. The molecular sieve is submerged in a liquid nitrogen trap as it works more effectively at lower temperatures because the oxygen can condense onto the MS pellets. After 10 minutes of cooling by liquid nitrogen, the sample bottle is closed and the MS pellets are then heated to 60 °C for 10 minutes, which causes the MS to release the O_2 as gas.

3.2.1.4   Isotope ratio mass spectrometer

The O_2 is then transferred the left bellow of the dual inlet system of the Delta^{Plus}XL isotope ratio mass spectrometer (Thermo Fisher Scientific). The dual inlet system has two bellows, the left one is filled with the sample O_2 which we want to measure, and the right bellow is filled with a reference O_2 gas. The isotopic composition of the sample is then measured by the isotope ratio mass spectrometer (IRMS) relative to the reference gas (VSMOW).

3.3 Results

3.3.1 Characteristation of the automated $\Delta^{17}O$ measurement system

3.3.1.1 Precision and stability of the $\Delta^{17}O$ measurement system

We carried out an experiment to investigate the experimental precision of the $\Delta^{17}O(CO_2)$ measurement system. To do this, we carried out a zero enrichment experiment. The O_2 zero enrichment experiment involves filling both bellows of the dual inlet system of the IRMS with the same O_2 gas. Therefore, the values of $\delta^{17}O$ and $\delta^{18}O$ should, in theory, be zero, as the isotopic composition of gas in both bellows is the same. The deviation from zero means that there is a difference between the bellows that has to be taken into account in the evaluation of the data. The results for the zero enrichment experiment are shown in Figures 3.3a, 3.3b, and 3.3c for $\delta^{17}O$, $\delta^{18}O$ and $\Delta^{17}O$, respectively. Each data point on the graph represents the average of 60 measurements cycles. The average values over all the zero enrichment experiments are, $\delta^{17}O = 0.035 \pm 0.0140\,‰$, $\delta^{18}O = 0.72 \pm 0.026\,‰$ and $\Delta^{17}O = -0.002 \pm 0.005\,‰$, with the errors equal to the standard error of the mean (SEM) multiplied by the Student's t-factor for 95% confidence (t). The experimental precision of the measurement system is given by the standard deviation of the measurements, $\delta^{17}O = 0.040\,‰$, $\delta^{18}O = 0.075\,‰$, and $\Delta^{17}O = 0.015\,‰$.

Figures 3.3a and 3.3b show that from measurement number 16 the results seem to have formed a new group which clusters more closely to 0. From experiment number 1 through to number 15, each bellow was filled with the same gas separately, however, from experiment number 16 to number 24 the sample bellow was filled with gas, and then the valves between the reference bellow and the sample bellow are opened, allowing the gas to equilibrate between the two bellows and the pressures to equalise in both bellows. This appears to have changed the isotopic composition measured between the bellows. Just focusing on these last 9 measurements leads to a different zero enrichment average, $\delta^{17}O =$ -0.004 $\pm$ 0.007 ‰, $\delta^{18}O =$ -0.011 $\pm$ 0.005 ‰, and $\Delta^{17}O = 0.002 \pm 0.005$ ‰ (SEM*t). The experimental precision of the measurement system is given by the standard deviation of the measurements, $\delta^{17}O =$ -0.015 ‰, $\delta^{18}O =$ -0.012 ‰, and $\Delta^{17}O = 0.011$ ‰. Therefore, as the results of the zero enrichment experiments from the total number of experiments are different from the results obtained from the last 9 measurements, the precise steps that are involved in the handling of this gas are important when looking at such small isotopic differences. The first method in which the bellows were filled separately (measurement number 1 to 15), led to a small isotope fractionation, evident from the fact that $\delta^{17}O$ and $\delta^{18}O$ are non zero. When the method of filling the bellows was changed to equilibrating the pressures between the two bellows (measurement number 15 to 24), the averages from the

zero enrichment experiments of $\delta^{17}O$ and $\delta^{18}O$ were closer to zero. The fractionation of the gas due to the initial sample admission method was mass-dependent, as it led to non zero values of $\delta^{17}O$ and $\delta^{18}O$, however the $\Delta^{17}O$ value was not significantly different from zero.

3.3.1.2 Investigating potential sources of fractionation in the $\Delta^{17}O$ measurement system

For the next system check, the isotopic composition of O_2 is measured after it has passed through the molecular sieve (MS) as well as when it is connected directly to the dual inlet system, in order to investigate whether any fractionation occurs due to O_2 passing through the MS. The isotopic composition of O_2 is also measured after it has been heated at 750 °C for 2 hours in the quartz exchange reactor with a platinum catalyst, to investigate whether any fractionation occurs due to interaction with the reactor/catalyst.

Figures 3.4a, 3.4b and 3.4c show the $\delta^{17}O$, $\delta^{18}O$ and $\Delta^{17}O$ compositions of the O_2 measured, respectively, under different experimental conditions. The teal dots show the actual isotopic composition of the oxygen, as these measurements correspond to the O_2 gas being directly connected to the dual inlet system which lets the gas into the IRMS. Figures 3.4a and 3.4b show that there is an offset between O_2 which has been directly measured and O_2 which has been passed through the MS, indicating that a small but significant fractionation occurs by passing the O_2 through the MS. The O_2 which has passed through the MS is isotopically heavier than O_2 which is directly connected to the dual inlet. This fractionation is mass-dependent, as there is no apparent offset between the MS and no MS measurements for $\Delta^{17}O$ (Figure 3.4c).

In attempt to investigate the cause of the fractionation, the isotopic composition of the O_2 was measured under different experimental conditions, when passed through the molecular sieve. For example, the freezing time on the molecular sieve was decreased from 15 minutes (red data points) to 10 minutes (black data points), which resulted in isotopically lighter O_2. The number of molecular sieve pellets used was also varied, as it was hypothesised that 3 pellets (the original number used) was not enough to adsorb all the O_2 gas present, so using a greater quantity of MS would result in more of the gas, and subsequently more lighter isotopes, being adsorbed on the MS. However, there was no apparent difference between the isotopic composition of the O_2 gas when 5 (green data points) or 8 (pink data points) MS pellets were used rather than 3 pellets. Silica gel was used as an adsorbent for one experiment instead of MS (orange data points), but this did not change the isotopic composition of the oxygen, compared to the use of molecular sieve.

We investigated whether the expansion process between valves 26 and 27 (explained in section 3.2.1.2) was responsible for the observed fractionation by directly expanding the gas into the MS (past valve 32). These experiments are depicted in Figure 3.4 with the
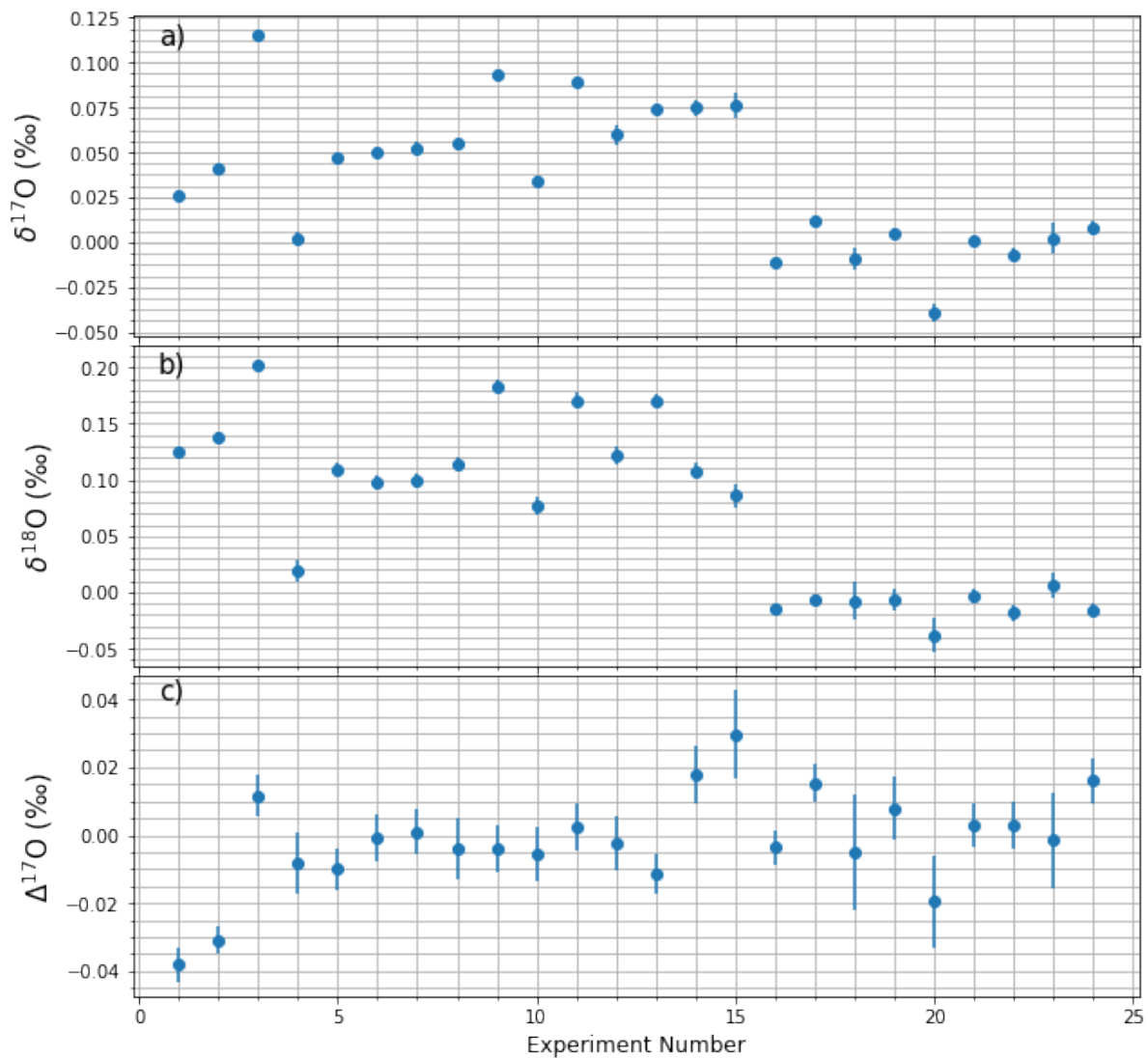
Figure 3.3: Results of the zero enrichment experiments of the IRMS, for (a) $\delta^{17}O$, (b) $\delta^{18}O$ and (c) $\Delta^{17}O$. In experiment numbers 1 to 15, each bellow was filled with gas separately. In experiments 16 to 24, the bellows were filled by equilibrating the gas between the two bellows. The error bars indicate the standard error of the mean for the particular measurement.
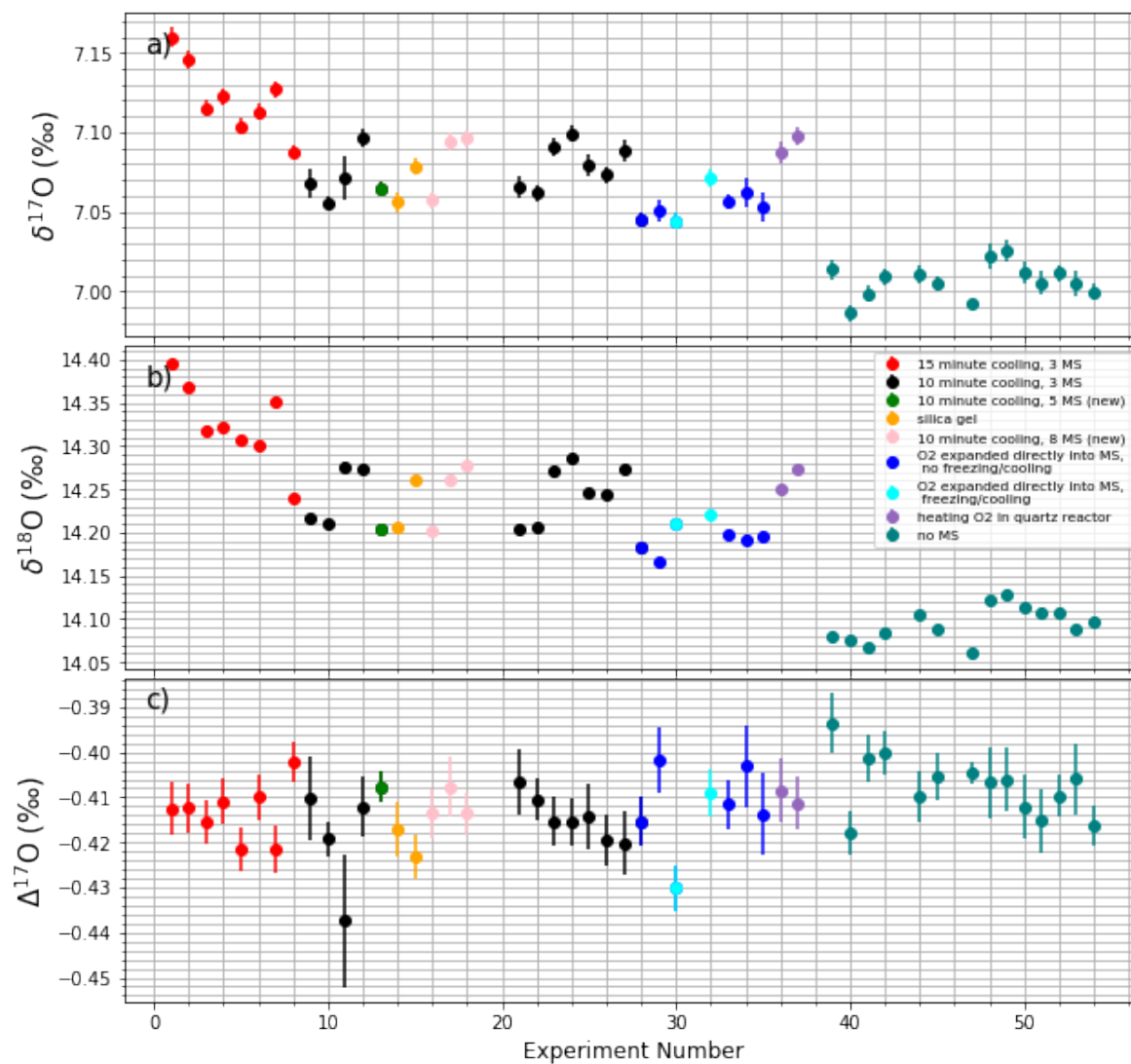
Figure 3.4: (a) $\delta^{17}O$, (b) $\delta^{18}O$, and (c) Δ^{17} of O₂ for several different experimental scenarios, which are indicated in the legend. The values are vs VSMOW. The error bars indicate the standard error of the mean for the particular measurement.

light blue and dark blue data points. It appears that this lowered the isotopic composition slightly compared to expanding between valves 26 and 27 (Figures 3.4a and 3.4b), however, not enough to close the offset gap in the $\delta^{17}O$ and $\delta^{18}O$ values between MS and no MS experiments, therefore this does not explain the observed fractionation.

Two experiments to investigate if fractionation occurs due to heating the gas in the exchange reactor over the platinum catalyst were carried out. The O_2 gas was heated in the exchange reactor at 750 °C for 2 hours, after which the gas is passed through liquid nitrogen traps 3 and 4, and the O_2 is cooled on the MS pellets for 10 minutes, then passed into the IRMS for measurement. These experiments are depicted in Figures 3.4a, 3.4b and 3.4c by purple data points. From these measurements we can conclude that no noticeable fractionation of O_2 happens due to interaction with the quartz (SiO_2) reactor, as the results are within the experimental errors of the results with 10 minutes cooling on the MS (black data points).

Considering the results of the experiments in Figures 3.4a and 3.4b, it was concluded that the offset between the isotopic composition measured between no MS and MS is caused primarily by the interaction of the oxygen with the molecular sieve. As the offset between the isotopic composition of O_2 which has been directly measured by the IRMS and O_2 which has been passed through a MS with 10 minutes cooling is known, we can correct for it in the values of $\delta^{17}O$ and $\delta^{18}O$ of O_2 which will be measured. The offset in $\delta^{17}O$ is 0.065 ‰, the offset in $\delta^{18}O$ is 0.134 ‰, and the offset in $\Delta^{17}O$ is -0.007 ‰. These values correspond to the difference between the average of the teal data points and the average the other coloured data points (excluding the red data points, which correspond to 15 minutes of cooling on the MS), in Figures 3.4a, 3.4b, and 3.4c, respectively. The offset observed for $\Delta^{17}O$ is smaller than the normal measurement precision, however, for consistency and because it is the mean of many data points, the offset should still be subtracted from any O_2 measurements taken.

3.3.2 Determination of the Fractionation Factors for CO_2-O_2 Isotope Exchange Reaction

The aim of the experiments described in this section is to find the fractionation factor of the CO_2-O_2 isotope exchange reaction at 750 °C, and to investigate how the fractionation factor varies with reaction temperature.

3.3.2.1 Investigating equilibrium reaction time of the CO_2-O_2 exchange reaction at three different reaction temperatures

First, it is necessary to know how long the exchange reaction between CO_2 and O_2 must proceed before isotopic equilibrium is reached. Reaction experiments are therefore carried out
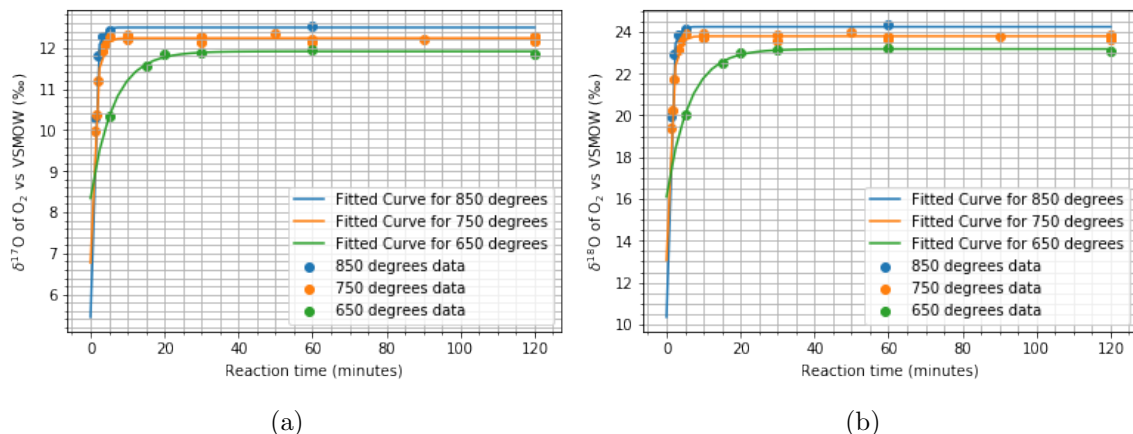
(a)   (b)

Figure 3.5: $\delta^{17}O(O_2)$ (a) and $\delta^{18}O(O_2)$ (b) after CO_2-O_2 exchange on a platinum sponge catalyst in a quartz reactor, for reaction temperature of 650 °C, 750 °C and 850 °C, against reaction time. The data are fitted to exponential curves. For Figure (a), the curves have equations $\delta^{17}O(t) = 11.913 - 3.572 \exp(-0.162t)$ for 650°C, $\delta^{17}O(t) = 12.237 - 5.185 \exp(-0.789t)$ for 750°C, and $\delta^{17}O(t) = 12.495 - 7.041 \exp(-1.160t)$ for 850°C. For Figure (b), the curves have equations $\delta^{18}O(t) = 23.178 - 7.074 \exp(-0.163t)$ for 650°C, $\delta^{18}O(t) = 23.795 - 10.045 \exp(-0.790t)$ for 750°C, and $\delta^{18}O(t) = 24.240 - 13.888 \exp(-1.178t)$ for 850°C.

at 650 °C, 750 °C and 850 °C, for various reaction times, and the final isotopic composition of O_2 is measured on the IRMS. The results are shown in Figures 3.5a and 3.5b.

Figures 3.5a and 3.5b show that increasing the reaction temperature increases the equilibrium isotopic composition of O_2 and decreases the reaction time necessary for equilibrium to be reached. Each data set for each of the three reaction temperatures is fit with an exponential curve of the form $y = A + B \exp(kt)$, where A is the final isotopic composition ($\delta^{17}O$ or $\delta^{18}O$) of O_2 at equilibrium, where $A + B$ is the isotopic composition of O_2 at $t = 0$, k is the rate constant of the reaction, and t is the reaction time. From these curve fits, the equilibrium values of $\delta^{17}O$ and $\delta^{18}O$ of O_2 at 650°C are $\delta^{17}O = 11.913$ ‰ and $\delta^{18}O = 23.178$ ‰, at 750°C are $\delta^{17}O = 12.237$ ‰ and $\delta^{18}O = 23.795$ ‰, and at 850°C are $\delta^{17}O = 12.495$ ‰ and $\delta^{18}O = 24.240$ ‰.

3.3.3 Temperature dependence of the fractionation factors of CO_2-O_2 exchange

Several experiments investigating the temperature dependence of the fractionation factors of the CO_2-O_2 exchange are carried out. As shown in Figure 3.7, equilibrium is reached after 120 minutes for 650 °C, 750 °C and 850 °C, therefore, the fractionation factor temperature dependence experiments are carried out for a reaction time of 120 minutes, with temperatures of 500 °C, 650 °C, 750 °C, 800 °C, 850 °C and 900 °C.

Table 3.1 shows the fractionation factors (α values) at 750 °C. This is the temperature

at which most replicate experiments were performed, as this was the reaction temperature which would have been used when measuring the isotopic composition of CO_2 from air samples. Table 3.1 shows the values of $\delta^{17}O(O_2)_f$, $\delta^{18}O(O_2)_f$, $\delta^{17}O(CO_2)_f$, $\delta^{18}O(CO_2)_f$, β (ratio of mass of CO_2 to O_2), $^{17}\alpha$ and $^{18}\alpha$, over 12 experimental replications. The averages, standard deviations and reproducibilities of each of the variables over the 12 experimental repeats are given in the last three rows of Table 3.1. The reproducibility of the data is reported as the standard error of the mean (SEM) times by the Student's t-factor to cover the 95% confidence interval (t). Table 3.1 reports the average α values for 750 °C as $^{17}\alpha = 1.00047 \pm 0.00001$ and $^{18}\alpha = 1.00044 \pm 0.00002$ (errors are SEM*t).

	$\delta^{17}O(O_2)$ final	$\delta^{18}O(O_2)$ final	$\delta^{17}O(CO_2)$ final	$\delta^{18}O(CO_2)$ final	β	$^{17}\alpha$	$^{18}\alpha$
	12.304	24.328	12.827	24.848	1.043	1.00052	1.00051
	12.138	23.980	12.608	24.454	0.969	1.00046	1.00046
	12.138	23.980	12.608	24.454	0.969	1.00046	1.00046
	12.352	24.407	12.811	24.829	1.050	1.00045	1.00041
	12.266	24.265	12.741	24.670	1.019	1.00047	1.00040
	12.143	24.021	12.604	24.413	0.969	1.00046	1.00038
	12.087	23.902	12.563	24.344	0.951	1.00047	1.00043
	12.226	24.162	12.694	24.606	1.002	1.00046	1.00043
	12.248	24.204	12.709	24.636	1.009	1.00046	1.00042
	12.333	24.364	12.786	24.788	1.041	1.00045	1.00041
	12.187	24.051	12.677	24.609	0.991	1.00048	1.00054
	12.228	24.148	12.701	24.636	1.003	1.00047	1.00048
	12.201	24.115	12.668	24.555	0.992	1.00046	1.00043
	12.296	24.319	12.757	24.706	1.028	1.00046	1.00038
Average	12.232	24.174	12.704	24.623	1.005	1.00047	1.00044
Std. Dev.	0.080	0.158	0.081	0.154	0.031	0.00002	0.00005
SEM * t	0.039	0.078	0.040	0.076	0.015	0.00001	0.00002

Table 3.1: CO_2-O_2 isotopic exchange at reaction temperature of 750 °C. Values of δ are in ‰ and vs VSMOW. The reproducibility is given in the last row, and is defined as the standard error of the mean times Student's t-factor for 95% confidence.

Three additional reactions at 750 °C were carried out to see if the initial value of $\delta^{17}O(CO_2)$ could be obtained using the values of $^{17}\alpha$ and $^{18}\alpha$ calculated for 750 °C, $^{17}\alpha = 1.00047$, $^{18}\alpha = 1.00044$. The results are shown in Table 3.2. The initial value of $\delta^{17}O(CO_2)$ obtained is 17.899 ± 0.005 ‰ (SEM times Student's t-factor for 95 % confidence) vs VSMOW, the true initial value of $\delta^{17}O(CO_2)$ is 17.904 ‰ vs VSMOW, which is within the error of the value obtained using the α values measured in this experiment (Table 3.1). So we can confirm that using the fractionation factors in Table 3.1, we can obtain an accurate value for $\delta^{17}O$ of CO_2 from samples.

	$\delta^{17}O(O_2)$ final	$\delta^{18}O(O_2)$ final	$\delta^{17}O(CO_2)$ final	$\delta^{18}O(CO_2)$ final	$\delta^{17}O(CO_2)$ initial
	12.27	24.258	12.743	24.706	17.896
	12.156	24.034	12.628	24.482	17.898
	12.232	24.177	12.704	24.625	17.902
Average	12.220	24.156	12.685	24.594	17.899
Std. Dev.	0.058	0.113	0.113	0.058	0.003
SEM * t	0.098	0.191	0.098	0.191	0.005

Table 3.2: CO_2-O_2 isotopic exchange at reaction temperature of 750 °C, using $^{17}\alpha = 1.00047$ and $^{18}\alpha = 1.00044$. Values are in ‰ and vs VSMOW. The reproducibility is given in the last row, and is defined as the standard error of the mean times Student's t-factor for 95% confidence.

Isotope exchange reaction experiments were also carried out at reaction temperatures of 500 °C, 650 °C, 800 °C, 850 °C and 900 °C. The values of $\delta^{17}O(O_2)_f$, $\delta^{18}O(O_2)_f$, $\delta^{17}O(CO_2)_f$, $\delta^{18}O(CO_2)_f$, β (ratio of mass of CO_2 to O_2), $^{17}\alpha$ and $^{18}\alpha$ measured from these experiments are given in Table 3.3. The averages, standard deviations and reproducibilities (SEM * t) are given for each temperature (apart from 500°C and 900°C, as only one experiment was carried out at these two temperatures).

Temp. (°C)	$\delta^{17}O(O_2)$ final	$\delta^{18}O(O_2)$ final	$\delta^{17}O(CO_2)$ final	$\delta^{18}O(CO_2)$ final	β	$^{17}\alpha$	$^{18}\alpha$
500	7.441	14.923	17.495	33.875	1.061	1.00998	1.01867
650	11.910	23.521	12.911	25.057	0.982	1.00099	1.00150
	11.809	23.339	12.974	25.165	0.974	1.00115	1.00178
Average	11.859	23.430	12.943	25.111	0.975	1.00107	1.00164
Std. Dev.	0.072	0.129	0.045	0.077	0.006	0.00012	0.00020
SEM * t	0.320	0.574	0.200	0.342	0.025	0.00051	0.00090
800	12.413	24.518	12.671	24.566	1.033	1.00025	1.00005
	12.265	24.227	12.490	24.223	0.971	1.00022	1.00000
	12.478	24.661	12.676	24.559	1.047	1.00020	0.99990
Average	12.385	24.468	12.612	24.449	1.017	1.00022	0.99998
Std. Dev.	0.109	0.221	0.106	0.196	0.040	0.00003	0.00007
SEM * t	0.184	0.373	0.179	0.330	0.179	0.00005	0.00012
850	12.552	24.769	12.477	24.207	1.022	0.99993	0.99945
	12.513	24.227	12.490	24.223	0.971	1.00022	1.00000
	12.441	24.611	12.441	24.081	0.995	1.00000	0.99948
	12.406	24.505	12.450	24.140	0.990	1.00004	0.99964
Average	12.478	24.652	12.472	24.174	1.007	0.99999	0.99953
Std. Dev.	0.066	0.119	0.037	0.081	0.018	0.00005	0.00009
SEM * t	0.078	0.140	0.043	0.095	0.021	0.00006	0.00010
900	12.596	24.877	12.434	24.102	1.022	0.99984	0.99924

Table 3.3: CO_2-O_2 isotopic exchange at reaction temperatures 500°C, 650°C, 800°C, 850°C and 900°C. Values of δ are in ‰ and vs VSMOW. The reproducibility of each experiment is given in the row "SEM * t", and is defined as the standard error of the mean times Student's t-factor for 95% confidence.

3.4   Discussion

3.4.1   Fractionation of O_2 due to interaction with the molecular sieve

Interaction of O_2 with MS can cause fractionation according to Abe (2008). However, in this paper the isotopic composition of the O_2 passed through the MS is lower than that of O_2 not passed through MS, which is the opposite to our result (see Figure 3.4). In the paper it is hypothesised that the O_2 which has passed through the MS is isotopically lighter because the lighter O_2 molecules are expected to be preferentially desorbed from the MS when it is heated, leaving behind the heavier isotopes in the pores of the MS. However, the results of the paper by Abe (2008) could be due to the particular experimental setup and conditions used by the author, and not a universal property of the MS-O_2 system. However, we still follow the suggestion of heating the MS at 60°C for 10 minutes post freezing in order to reduce the amount of fractionation occurring at the MS (Abe 2008).

3.4.2 Investigating the reaction rate constant of the CO_2-O_2 isotope exchange reaction at 500°C

In the experiments investigating the temperature dependence of the fractionation factor of the CO_2-O_2 isotope exchange reaction (section 3.3.3, Table 3.3), it can be seen than the fractionation factors decrease as the reaction temperature is increased. For a reaction temperature of 500°C, the values of $\delta^{17}O$ and $\delta^{18}O$ for CO_2 and O_2 are much closer to the initial values of CO_2 and O_2 compared to the other reaction temperatures (Table 3.3), suggesting that isotopic equilibrium may not be reached by 120 minutes for 500°C. To find if equilibrium is reached by 120 minutes for 500°C, the rate constant of the reaction at 500°C needs to be found. This can be calculated from the Arrhenius equation,

$$k = A \exp\left(\frac{-E_a}{RT}\right), \tag{3.4}$$

where, k is the reaction rate constant, A is the pre-exponential factor, E_a is the activation energy (in units of RT), R is the universal gas constant and T is the reaction temperature (in Kelvin) (Arrhenius 1889). The Arrhenius equation demonstrates that the rate of a reaction is dependent on the reaction temperature.

The values of k for the different reaction temperatures, T, are found from the exponential curve fits of $\delta^{17}O(O_2)$ and $\delta^{18}O(O_2)$ against reaction time (Figure 3.5), as each curve has an equation in the form $y = A + B\exp(kt)$, with k being the rate constant (in units of minute^{-1}) and t being the reaction temperature (in units of minutes). The values of k, for $\delta^{17}O(O_2)$ (k_{17}) and $\delta^{18}O(O_2)$ (k_{18}), are given in Table 3.4.

Temperature (°C)	k_{17} (minute^{-1})	k_{18} (minute^{-1})
650	0.162 ± 0.023	0.163 ± 0.019
750	0.789 ± 0.070	0.790 ± 0.071
850	1.160 ± 0.085	1.178 ± 0.076

Table 3.4: The rate constant (k) for different reaction temperature, for $\delta^{17}O$ (k_{17}) and $\delta^{18}O$ (k_{18}), obtained from the exponential curve fit of $\delta^{17}O$ and $\delta^{18}O$ as a function of reaction time. The errors on k_{17} and k_{18} are the standard deviations.

Taking the natural logarithm of equation (3.4) gives,

$$\ln(k) = \ln(A) - \frac{E_a}{R}\left(\frac{1}{T}\right). \tag{3.5}$$

Plotting equation (3.5), using the rate constants from 650°C, 750°C and 850°C in table 3.4, results in Figure 3.6. The data points are fitted with the linear trend lines, $\ln(k_{17}) = -\frac{10375}{T} + 9.586$ and $\ln(k_{18}) = -\frac{10432}{T} + 9.652$. These equations are used to extrapolate the

rate constant at 500°C of $k_{17} = 0.0216 \pm 0.0909$ min^{-1} and $k_{18} = 0.0214 \pm 0.0947$ min^{-1} (errors are the standard deviations).
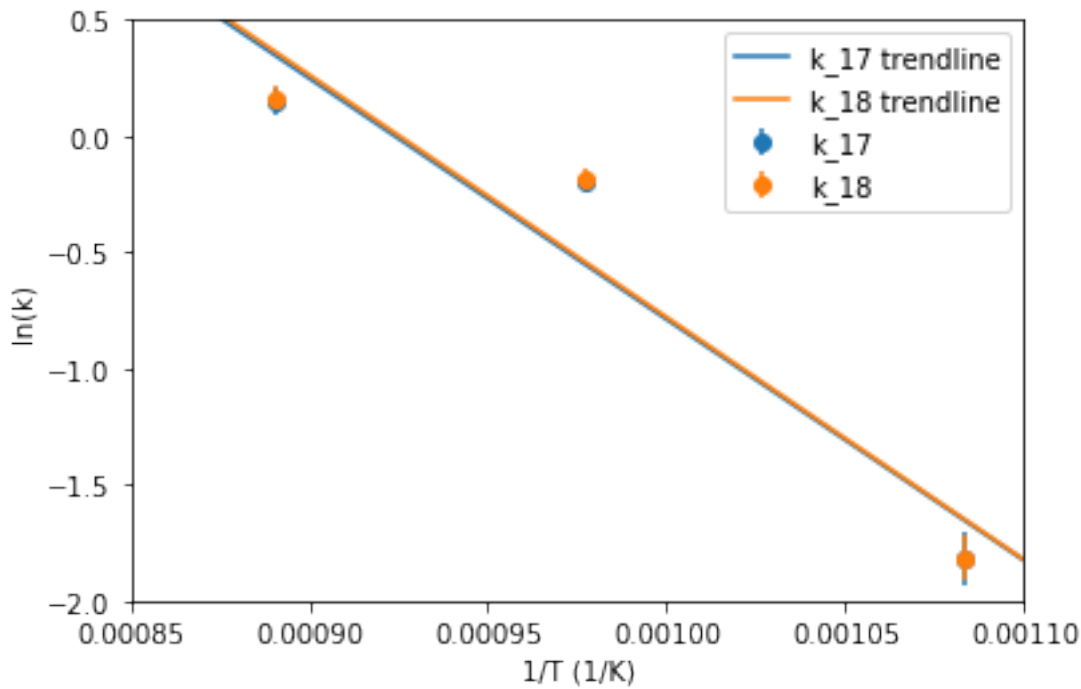

Figure 3.6: ln(k) vs inverse temperature (units are 1/Kelvin). The blue points represent the values of the δ^{17}O rate constant, the orange points represent the values of the δ^{18}O rate constant. The blue line is the linear line of best fit for the rate constants corresponding to δ^{17}O, with equation, $\ln(k) = -\frac{10375}{T} + 9.586$. The orange line is the linear line of best fit for the rate constants corresponding to δ^{18}O, with equation, $\ln(k) = -\frac{10432}{T} + 9.652$. The error bars are standard error of the mean times Student's t-factor for 95% confidence.

Using an average value of $k = 0.0215$ min^{-1} for δ^{17}O and δ^{18}O for a reaction temperature of 500°C, at 120 minutes $\exp(-kt) = 0.076$, meaning the isotopic composition of O_2 has only reached 92.4% of its final isotopic equilibrium value. Whereas when equilibrium is reached for 650°C (after approximately 45 minutes) the isotopic value of O_2 has reached 99.9% of its final equilibrium value. Therefore, it can be assumed that at a reaction temperature of 500°C, equilibrium has not been reached for a reaction time of 120 minutes, so we exclude the measurements of $^{17}\alpha$ and $^{18}\alpha$ at 500°C from our results.

However, extrapolating to a temperature of 500°C from Figure 3.6 may not yield a very accurate value of k as the error bars of the data points don't cross the linear trend line, and it is difficult to know how robust this trend is, given that there are only three data points. The R-squared values for both $\ln(k_{17})$ and $\ln(k_{18})$ is 0.911. As the Arrhenius relationship is a well known and tested relationship, our data should lie on a linear fit, within the error

bars. The linear fit does not lie within the error bars of the data points, indicating that there may be a systematic error within our results.

3.4.3 The temperature dependence of the fractionation factor: experimental vs theoretical

Theoretically calculated values of the fractionation factors, $^{17}\alpha$ and $^{18}\alpha$, of the CO_2-O_2 isotope exchange reaction across a temperature range of 0 to 1300°C are plotted in Figure 3.7a, with dark blue and dark pink data points, respectively. These theoretical values were calculated by Janssen (2020), which were recalculated from the results in Richet et al. (1977). These fractionation factors are calculated by finding the ratios of the molecular partition functions for CO_2 and O_2 before and after isotopic exchange (Richet et al., 1977). The $^{17}\alpha$ and $^{18}\alpha$ values are fitted with exponential functions of the form $y = A + B\exp(Cx)$. The equations of the curves fit to the theoretically calculated data are $^{17}\alpha = 1.00200 + 0.01885\exp(-0.00450T)$ and $^{18}\alpha = 1.00376 + 0.03523\exp(-0.00455T)$. The values of $^{17}\alpha$ and $^{18}\alpha$ measured in this study (Tables 3.1 and 3.3) are also plotted in Figure 3.7a, with light blue and pink data points, respectively. Figure 3.7a shows that there is an offset between the theoretically calculated values and the values found experimentally. The trend in the theoretically calculated values of α indicate how we would expect α found experimentally to behave at different temperatures, provided we assume our results follow the theory at a larger temperature range, but perhaps with on offset.

Figure 3.7b shows the results in Figure 3.7a but focused on the temperature range 600 to 900°C. The experimental data are fitted with linear trend lines with R^2 values of 0.993 for $^{17}\alpha$ and 0.992 for $^{18}\alpha$. The theoretically calculated results are shown in Figure 3.7b, and are also fitted with a linear trend line with an R^2 values of 0.988 for $^{17}\alpha$ and 0.986 for $^{18}\alpha$. The slopes of the $^{18}\alpha$ and $^{17}\alpha$ trend lines found experimentally and theoretically are presented in Table 3.5. From this table, it can be seen that the slopes of the experimental and theoretical trend lines are within one standard deviation for both $^{17}\alpha$ and $^{18}\alpha$.

The average offset shown in Figure 3.7 between the theoretical values and the experimental values of $^{17}\alpha$ is 0.00238 and of $^{18}\alpha$ is 0.00483. These values are calculated by extrapolating theoretically calculated α values along the trend lines of the theoretical values at temperatures of 650, 750, 800, 850 and 900 °C. The difference is taken between these values and the experimentally calculated values at each temperature. The average of these values is taken, and this is the offset between the experimental and theoretical fractionation factors. The offset between the $^{17}\alpha$ values is approximately half that of the offset between the $^{18}\alpha$ values, which indicates that the process that causes this offset is associated with a mass dependent fractionation. The reason for this offset is not yet fully understood, it could be an indication of real gas effects compared to ideal gas assumptions, which are used

|	Slope of the $^{17}\alpha$ trend line $(\times 10^{-6})$	Slope of the $^{18}\alpha$ trend line $(\times 10^{-6})$
Experimental	-4.735 ± 0.230	-9.113 ± 0.470
Theoretical	-4.690 ± 0.364	-8.665 ± 0.677

Table 3.5: Slopes of the trend lines of $^{17}\alpha$ and $^{18}\alpha$, experimentally calculated and theoretically calculated, over the temperature range 600 °C to 900 °C. The theoretical values are calculated by Janssen (2020), recalculated from the results of Richet et al. (1977). The errors on the α values are the standard errors.

in the theoretical calculations. Alternatively, there could be additional effects related to the handling of the gases, or inconsistencies between the isotopic scales of O_2 and CO_2.

One difference between the theoretically calculated values of $^{18}\alpha$ and the $^{18}\alpha$ measured in this study is that the theoretical values do not consider the presence of a reaction catalyst. However, this can not explain the offset between the values of $^{18}\alpha$ between our experiment and the theoretical values, as the presence of a catalyst would only increase the rate of the exchange reaction, but not affect the equilibrium values reached, as these are determined by thermodynamics, which does not change with the presence of a catalyst.
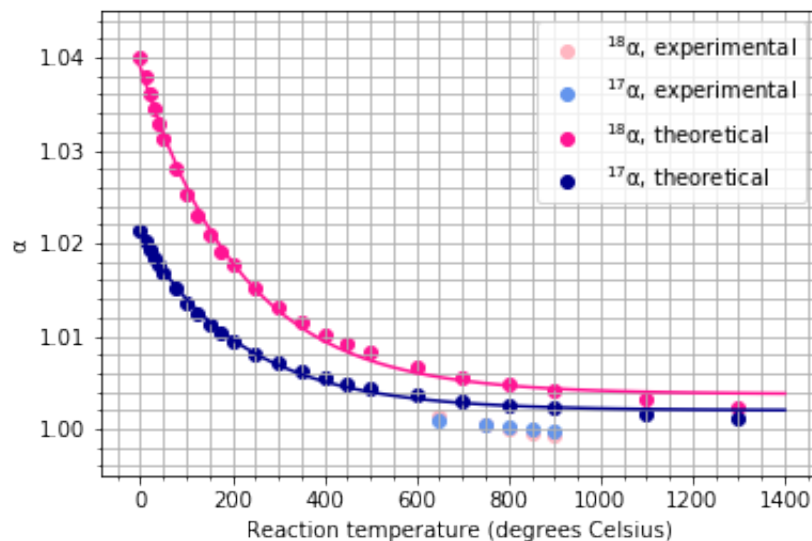
(a) $^{17}\alpha$ and $^{18}\alpha$ against reaction temperature, calculated from the measurements from this study (Tables 3.1 and 3.3). The values from Janssen (2020) are also shown, and fitted with exponential curves of the form $y = A + B\exp(Cx)$. The equations of the exponential curves are $^{17}\alpha = 1.00200 + 0.01885\exp(-0.00450T)$ and $^{18}\alpha = 1.00376 + 0.03523\exp(-0.00455T)$.
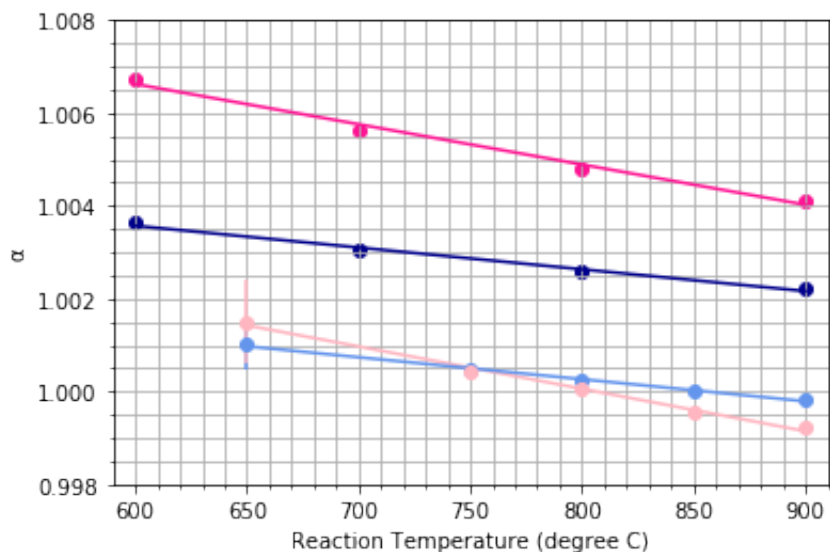
(b) $^{17}\alpha$ and $^{18}\alpha$ against reaction temperature, calculated from the measurements from this study (Tables 3.1 and 3.3), and theoretically calculated (Janssen 2020). Both data sets are fitted with linear trend lines, the equations of the trend lines of the experimental data points are $^{17}\alpha = -5 \times 10^{-6}\mathrm{T} + 1.0041$ and $^{18}\alpha = -9 \times 10^{-6}\mathrm{T} + 1.0073$, and the equations of the trend lines of the theoretically calculated values are $^{17}\alpha = -5 \times 10^{-6}\mathrm{T} + 1.0064$ and $^{18}\alpha = -9 \times 10^{-6}\mathrm{T} + 1.0118$. The error bars on the $^{17}\alpha$ and $^{18}\alpha$ experimental values are standard error of the mean times Student's t-factor for 95% confidence (see Tables 3.1 and 3.3 for errors). There are no error bars for 900 °C as there was only one experiment carried out at this temperature.

Figure 3.7

Part II: Modelling

Due to COVID-19, the laboratory was closed, and measurements of the isotopic composition of CO_2 from air samples could not be taken. Therefore, the scope of this thesis had to be revised, and so, in the second part of this thesis we use a coupled land-atmosphere model (Vilà-Guerau de Arellano & van Heerwaarden 2015) to simulate the diurnal evolution of $\Delta^{17}O(CO_2)$ in the atmospheric boundary layer (ABL). The $\Delta^{17}O(CO_2)$ signal has been implemented in the model by Koren (2020). In this study, the model is used to investigate the diurnal evolution of $\Delta^{17}O$ of CO_2 in the ABL and of $\Delta^{17}O$ of CO_2 in equilibrium with leaf water. Several sensitivity analyses are carried out to study how sensitive the modelled signal of $\Delta^{17}O(CO_2)$ is to changes in different meteorological conditions.

4.1 Methods

4.1.1 MXL model

The model used in this study is a mixed layer (MXL) model, which simulates a convective boundary layer coupled to the surface (Vilà-Guerau de Arellano & van Heerwaarden 2015). The model simulates the exchange of CO_2 and water between the biosphere (soil and vegetation) and the atmosphere, therefore allowing us to study biosphere-atmosphere feedbacks. An example of one of these feedbacks is the "heating-assimilation" feedback. This feedback states that an increase in the potential temperature will cause an increase in the uptake of CO_2 by the plant to be used in photosynthesis. This will decrease the concentration of CO_2 in the ABL, which will lead to reduced heating in the ABL, due to a reduced greenhouse effect, subsequently decreasing the potential temperature in the ABL. This is an example of a negative feedback loop. The diurnal cycle of the isotopologues of CO_2 and H_2O in the atmospheric boundary was simulated by Vilà-Guerau de Arellano et al. (2019), over a forest ecosystem. The $\Delta^{17}O(CO_2)$ signal in the atmospheric boundary layer was then implemented by Koren (2020). This implementation was done by simulating the $\Delta^{17}O$ signature of leaf water, as it is related to the $\Delta^{17}O$ signature of CO_2 in the ABL.

The $\Delta^{17}O$ of leaf water is determined from the xylem water isotopic signature ($\Delta^{17}O_x$) and the fractionation associated with transpiration of water (see equation 4.3 in section 4.2.3.1) (Koren et al. 2019).

This model simulates a day above Loobos forest. Loobos forest is primarily a pine tree forest situated in the east of the Netherlands, as shown with the red cross in Figure 4.1. It is an appropriate location to model, as there is a measurement tower reaching 1-2 m above the forest canopy, which allows the model runs to be validated and calibrated with measurements (see http://www.climatexchange.nl/ for more details). The model is calibrated using measurements of the isotopic composition of atmospheric CO_2 above the forest canopy, taken at Institute for Marine and Atmospheric research Utrecht (IMAU), using the measurement methods described in section 3.2.

Figure 4.1: A satellite image of the Netherlands, with the location of Loobos forest indicated with a red cross (Google Maps, 2020).

4.1.2 Sensitivity Analyses

The purpose of a sensitivity analysis is to investigate how sensitive a model is to a change in the initial value of a particular variable. In this study we are interested in what the effect of changing certain meteorological variables is on the $\Delta^{17}O$ value of leaf water and of CO_2 in the ABL. Meteorology affects the isotopic composition of leaf water, and consequently the isotopic composition of CO_2 in the ABL, as the relative humidity in the ABL is a key parameter which controls the leaf water isotopic composition. The Craig-Gordan model (Craig &

Gordon 1965) governs this relationship, and states that leaf water is more enriched in ^{18}O in conditions of reduced relative humidity, as there is a greater rate of evapotranspiration from the leaf, and the lighter water isotopes are preferentially evaporated over the heavier isotopes. Therefore, we predict that leaf water will be more enriched in ^{18}O in sensitivity cases with lower humidity. We present here four different sensitivity analyses for the MXL model, each has a different initial meteorological variable changed, and were chosen as they each influence the relative humidity of the ABL in different ways. The sensitivity cases are listed in table 4.1, the numbers in bold text indicate the main parameter which has been changed for that particular case, compared to the control.

	w (m^3/m^3)	dq_0 (g/kg)	θ_0 (K)	[CO$_2$] in ABL (ppm)	[CO$_2$] in FT (ppm)
Control	0.235	-0.1	288.15	460	420
Decreased soil moisture	**0.2**	-0.1	288.15	460	420
Decreased FT moisture	0.235	**-3.1**	288.15	460	420
Increased potential temperature	0.235	-1.02	**290**	460	420
Increased CO$_2$ concentration	0.235	-0.1	288.15	**750**	**710**

Table 4.1: The initial meteorological variables in each sensitivity case. Numbers in bold highlight the main variable which is changed in each case. For Sensitivity 2, the main variable change which defines this sensitivity analysis is the change in potential temperature, however the value of the specific humidity inversion at the boundary of the ABL and the FT, dq_0, is also changed relative to the control case, as we changed initial specific humidity in the ABL for this case, so that each sensitivity case has the same initial relative humidity. Therefore, to keep the water content in the FT the same as the control case, the magnitude of dq_0 needed to be increased.

In the first two sensitivity analyses in Table 4.1, the humidity in the ABL is directly decreased by two different methods. A local process is changed (decreasing soil water content (w)) and a change in the non-local meteorology is made (decreasing the moisture in the free troposphere (FT)), both of which lead to a decrease in the specific humidity in the ABL. A decrease in moisture in the FT is achieved by increasing the magnitude of the specific humidity inversion at the boundary of the FT and the ABL, dq_0. This leads to entrainment of dry air into the ABL. The next sensitivity analysis in table 4.1 involves increasing the initial potential temperature in the ABL (θ_0). Warmer air can hold more moisture, so we increase the specific humidity in the ABL in this sensitivity case. For the final sensitivity analysis in table 4.1, the concentration of CO$_2$ in the ABL and in the FT is increased, which is simulating a future climate change scenario. Increasing the concentration of CO$_2$ will decrease the concentration of open stomata in the leaves, as an equal, or greater, concentration of CO$_2$ can be assimilated at a reduced stomatal conductance. This leads to reduced evaporation from the leaves, and hence the humidity in the ABL decreases. More information on the different model inputs for each of the sensitivity cases is given in

Appendix A.

4.2 Results and Discussion

The aim of this study is to investigate the diurnal evolution of $\Delta^{17}O$ of CO_2 in the atmospheric boundary layer, and the contributions which make up this signal, under the different sensitivity analyses. We will first investigate how several meteorological variables are changed under the different sensitivity analyses. This is important as the differences in meteorology drives the differences in the isotopic signals between the sensitivity analyses, due to how the meteorology impacts the relative humidity in the ABL. Next, we study how the CO_2 fluxes between the plant and the ABL (assimilation flux), and the soil and the ABL (soil respiration flux) change between the different sensitivity analyses. Then the isotopic signatures of leaf water and of CO_2 in equilibrium with leaf water are investigated. The isofluxes between the surface and the ABL are then investigated, where a CO_2 isoflux is defined as the flux of CO_2 between a source and the ABL multiplied by its isotopic composition. An isoflux is the means by which the plant and the soil transfers its isotopic composition into the ABL. These isofluxes from the surface are then used to help explain the isotopic composition of CO_2 in the ABL. The temporal budgets of $\delta^{18}O$ and $\Delta^{17}O$ of CO_2 in the ABL are then presented, and their individual contributions from the surface and from entrainment are discussed. These signals are all investigated under each of the sensitivity analyses.

4.2.1 Meteorological variables

Each sensitivity analysis described in Table 4.1 corresponds to changing an atmospheric variable. Figure 4.2 is from van Heerwaarden et al. (2009), and shows several meteorological feedback loops in the coupled land-atmosphere system. This figure is used to describe how the meteorological variables evolve under each of the sensitivity analyses compared to the control case. The analysis for each of the sensitivity cases is discussed in the bullet points below.

- Reduced soil moisture: under this sensitivity case, less energy is partitioned into latent heat flux (LE) at the surface, and so more is partitioned into sensible heat flux (H). Following the "heating" feedback loops, the ABL height (h) increases, and the potential temperature (θ) increases. Following the "moistening" feedback loop, decreasing LE leads to a decrease in the specific humidity (q).

- Reduced moisture in the free troposphere: in this case, the water content in the FT is decreased, reducing the greenhouse effect, and so decreasing the sensible heat flux (H).
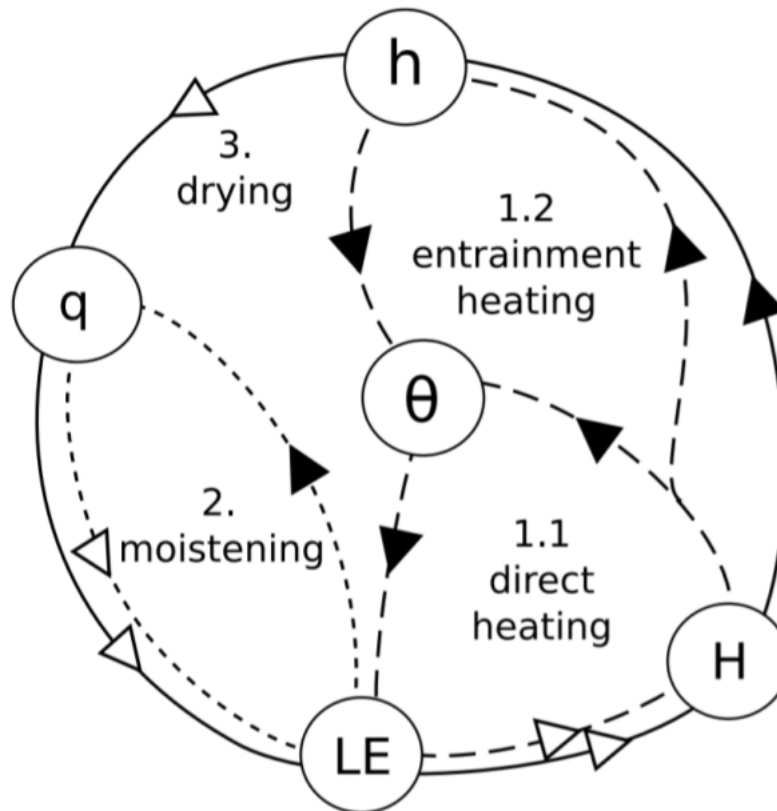
33

Figure 4.2: Meteorological feedbacks in a coupled land-atmosphere system. Black arrows represent a positive relationship, and white arrows represent a negative feedback. There are several feedback loops indicated with different line types, which are separately described in van Heerwaarden et al. (2009). LE is the latent heat energy (or evapotranspiration), H is the sensible heat flux, θ is the potential temperature, h is the ABL height, and q is the specific humidity in the ABL. This figure is taken directly from Heerwaarden, et al. (2009), Figure 1

Following the "heating" feedback loops, θ and h are decreased. As there is a decrease in specific humidity in the FT, this dry air is entrained into the ABL, reducing q in the ABL.

- Increased initial potential temperature: in this case θ is increased, this leads to an increase in latent heat energy, through the "direct heating" feedback loop (as warmer air can hold more moisture than cooler air), which consequently leads to a decrease in sensible heat flux. Therefore, following the "drying" feedback loop, h decreases, leading to an increase in q.

- Increased CO_2 concentration: under this sensitivity case, the greenhouse effect is increased, leading to an increase in H. Following the "heating" feedback loops, h and θ are increased. Following the "drying" feedback loop, q is decreased.

The meteorological outputs of potential temperature, ABL height, specific humidity, and relative humidity from the model are shown in Figure 4.3 for each of the sensitivity cases. The discrepancies between the sensitivity analyses in the relative humidity (RH) graph in Figure 4.3d, are explained using the same reasoning as that used for the discrepancies between the specific humidity, however the increased potential temperature case decreases below the control at approximately 7 UTC. This is because warmer air holds more moisture than colder air, which can result in a lower RH than the control case.
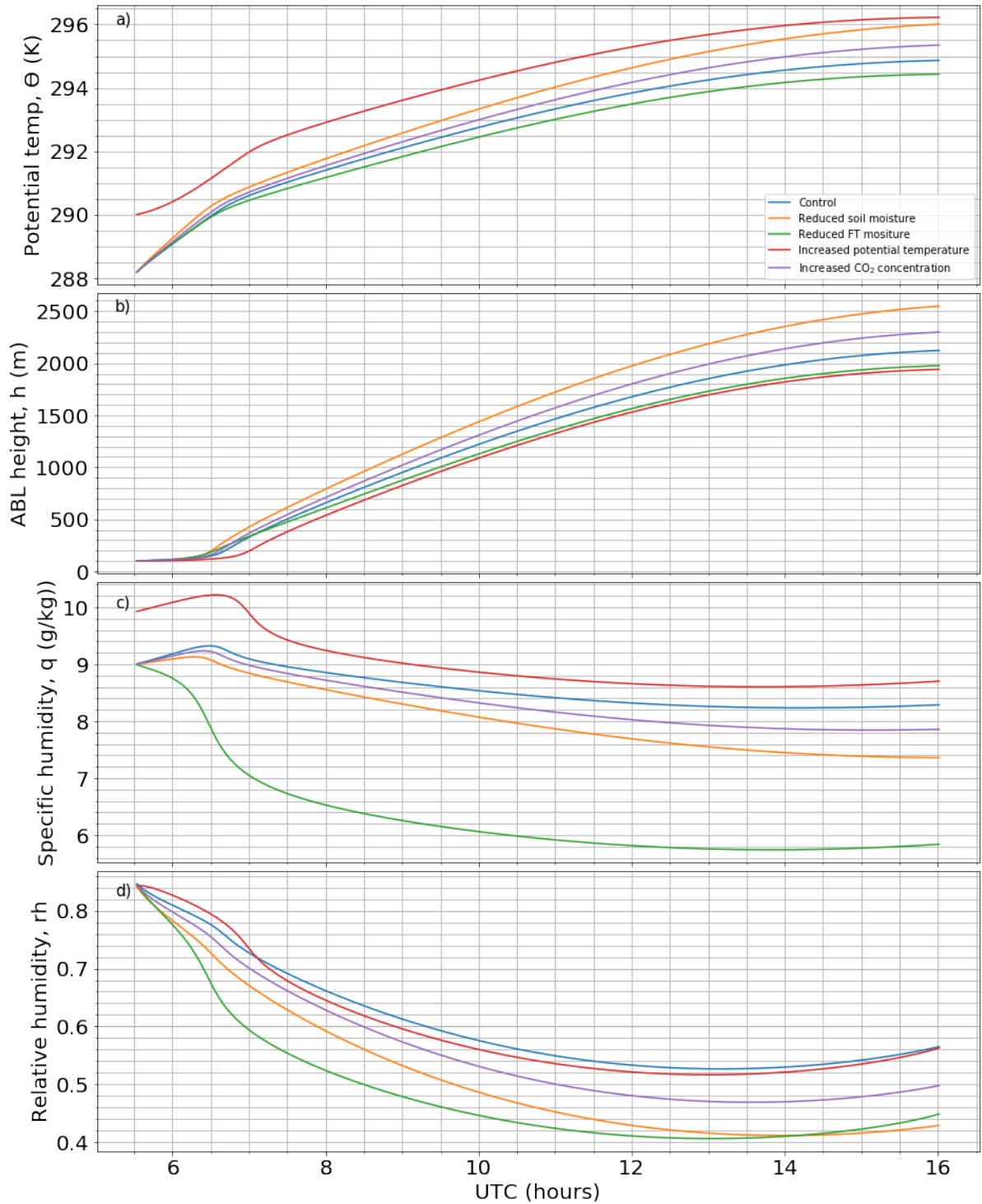
Figure 4.3: Diurnal evolution (from 5:30 to 16:00) of a) potential temperature (θ), b) atmospheric boundary layer height (h), c) specific humidity (q), and d) relative humidity (rh), across the different sensitivity analyses described in table 4.1. The different coloured lines refer to different sensitivity cases; blue: control, orange: reduced soil moisture, green: reduced FT moisture, red: increased potential temperature, purple: increased CO_2 concentration.

4.2.2 CO$_2$ Surface Fluxes

It is important for this study to understand how the CO$_2$ fluxes between the plant and the ABL (assimilation), and the soil and the ABL (soil respiration) change across each of the sensitivity analyses. In order to investigate this, we add assimilation and soil respiration feedback loops to the meteorological feedback loops from van Heerwaarden et al. (2009) (Figure 4.2). These additional feedback loops are presented in Figure 4.4, with a different colour corresponding to a different feedback loop. Each of the additional feedback loops are described in the bullet points below.

- Temperature-assimilation feedback: this is the blue feedback loop in Figure 4.4. An increase in potential temperature, θ, will cause an increase in the assimilation rate, An, which consequently decreases the CO$_2$ concentration in the ABL. A decrease in CO$_2$ concentration will lead to reduced heating (H) in the ABL due to a reduced greenhouse effect. This leads to a decrease in θ. This is a negative feedback loop.

- CO$_2$-assimilation feedback: this is the green feedback loop in Figure 4.4. Under higher ABL CO$_2$ mixing ratios, the stomatal resistance increases (Kruijt et al. 2008), as the CO$_2$ gradient between the inside of the leaf and the outside of the leaf is greater. This means that the same amount of CO$_2$ can diffuse into the leaf with a smaller stomatal aperture (Super et al. 2015). The increased stomatal resistance alone will limit assimilation, however this is compensated by the higher CO$_2$ concentration.

- Humidity-assimilation feedback: this is the pink feedback loop in Figure 4.4. Increased humidity (q), will decrease the water vapour pressure deficit (WVPD) in the ABL, which leads to a decrease in the stomatal resistance, as the leaf will open more stomata in response to less dry conditions. Therefore, more CO$_2$ can be assimilated, which leads to a decrease in the CO$_2$ concentration in the ABL, and consequently, a decrease in the sensible heat flux (H). Following the "drying" feedback loop, leads to an increase in specific humidity. This is a positive feedback loop.

- Temperature-soil-respiration feedback: this is the red feedback loop in Figure 4.4. Greater temperatures lead to greater soil respiration rates (Rs). This is a positive feedback loop as increasing the soil respiration increases the ABL CO$_2$ mixing ratio, which increases heating at the surface (H), hence leading to greater soil respiration.

- Stomatal resistance-temperature feedback: this is the brown feedback loop. Vegetation has an optimum temperature, beyond which stomatal resistance is increased (Noilhan & Mahfouf 1996). With more stomata closed, transpiration is limited, thereby reducing evapotranspiration (LE). Consequently, H and θ are increased, increasing stomatal resistance, if the temperature exceeds an optimum temperature.
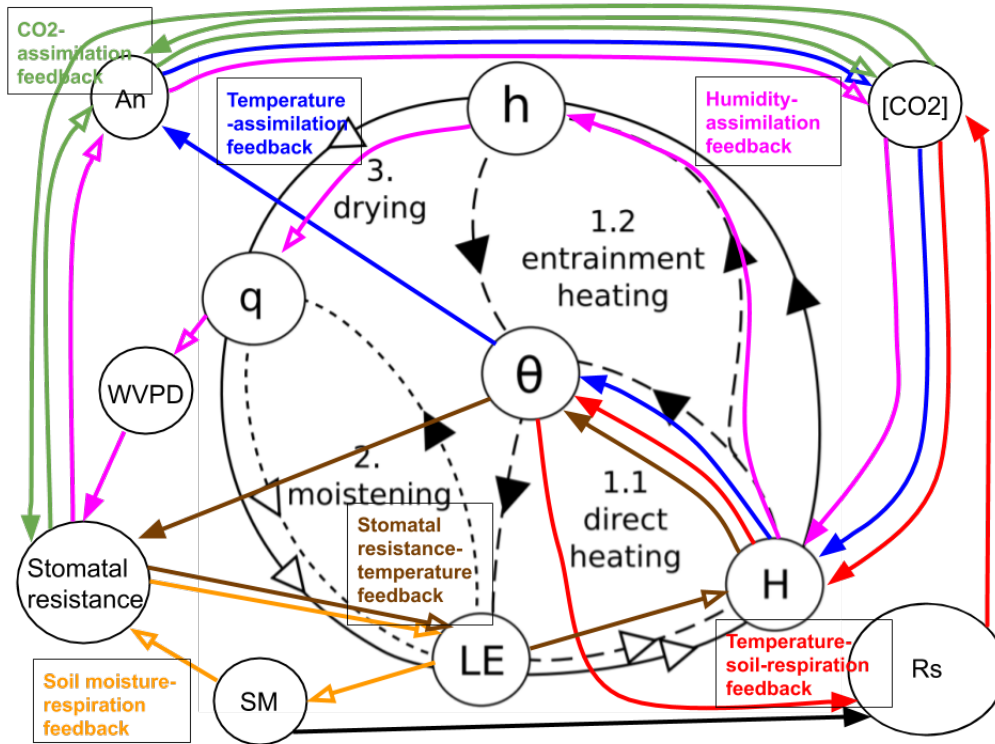
37

Figure 4.4: Assimilation and soil respiration feedback loops in the coupled land-atmosphere system. The figure is adapted from Figure 1 of van Heerwaarden et al. (2009). The closed arrows indicate a positive relationship, the open arrows represent a negative relationship. The different feedback loops are indicated using different colours; temperature-assimilation feedback is blue, CO_2-assimilation feedback is green, humidity-assimilation feedback is pink, temperature-soil-respiration feedback is red, stomatal resistance-temperature feedback is brown, and soil moisture-respiration feedback is orange. See the text for the explanation on each of the new feedback loops.

Therefore this is a positive feedback loop, providing the temperature is greater than the optimum temperature of the particular vegetation.

- Soil moisture-respiration feedback: this is the orange feedback loop in Figure 4.4. As a response to drying soils, the stomata close to prevent further water loss (the stomatal resistance increases). This causes a reduction in transpiration, and thereby also a reduction in evapotranspiration (LE). As evapotranspiration includes both transpiration and evaporation from soil, there is reduced evaporation from the soil, resulting in an increase in soil moisture (Super et al. 2015). This is a negative feedback loop.

The turbulent CO_2 fluxes, $\overline{w'c'}$, between the surface and the ABL, are shown in Figure 4.5. This figure shows $\overline{w'c'}$ due to (a) plant assimilation, (b) soil respiration, and (c) total surface flux (assimilation plus respiration). In Figure 4.5 the sign convention is such
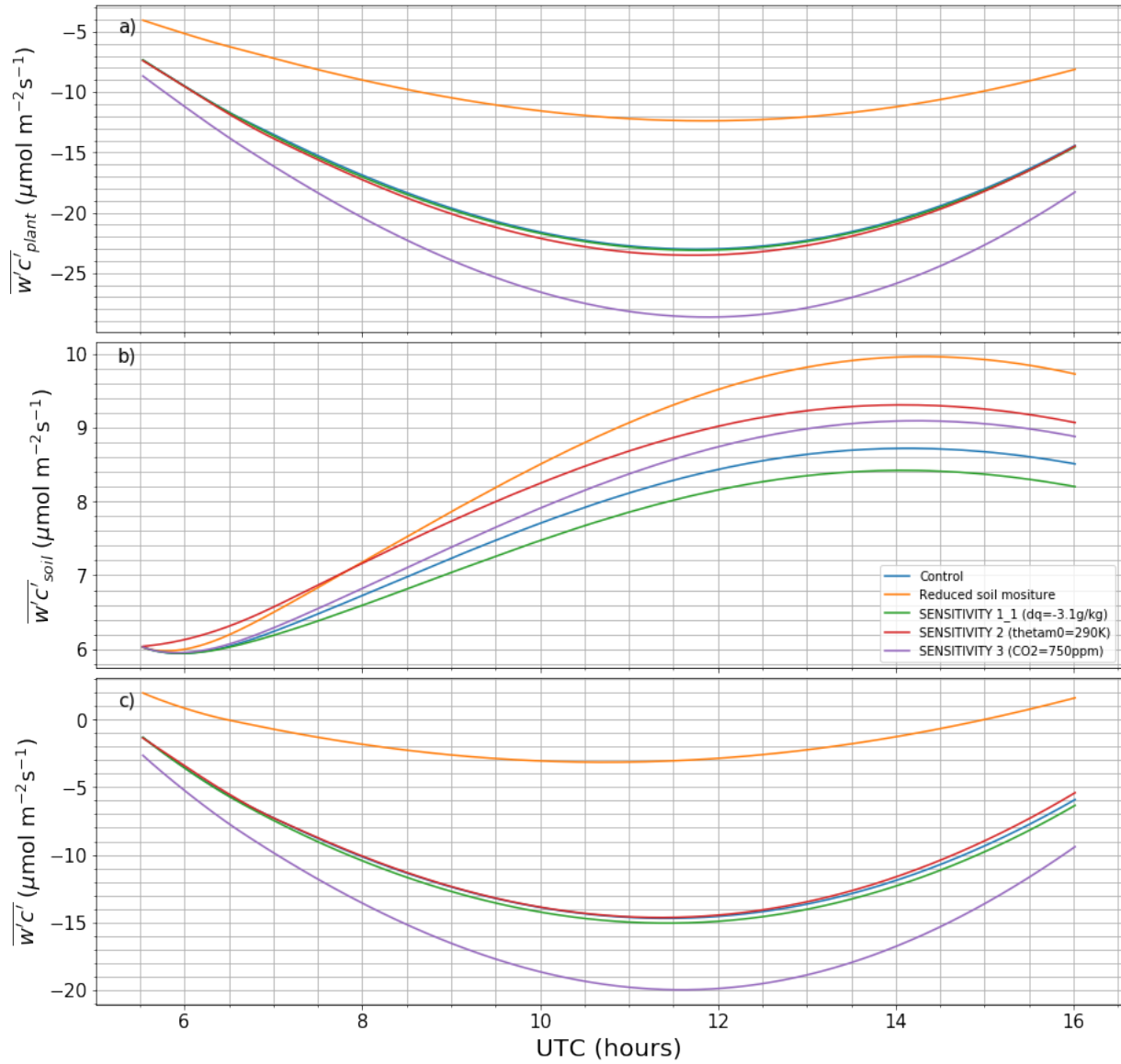
Figure 4.5: Diurnal evolution of the CO_2 fluxes $\overline{w'c'}$ due to a) plant assimilation, b) soil respiration, and c) assimilation plus respiration, under the different sensitivity analysis cases, in units μmol m^{-2}s^{-1}. A positive (negative) value of the flux indicates that CO_2 is being added (removed) from the ABL.

that a positive (negative) flux is adding (removing) CO_2 from the ABL. The values of the assimilation flux are always negative, as the process of assimilation is removing CO_2 from the ABL. The values associated with the soil respiration flux values are always positive, as this process is adding CO_2 to the ABL. The total CO_2 flux in Figure 4.5c shows mainly negative values (with exception of the reduced soil moisture in the morning and evening), with a maximum magnitude at approximately 11:30 UTC when the rate of photosynthesis is maximised.

The formulation for the assimilation flux is described in Appendix 3 of Vilà-Guerau de Arellano & van Heerwaarden (2015). It is based on a coupled stomatal conductance and carbon (A-gs) model formulation, which describes the uptake of CO_2 by the plant as a function of plant physiological parameters and environmental parameters (e.g. ABL CO_2 mixing ratio, photosynthetically active radiation). The formulation for the soil respiration flux used in the model is a function of the soil temperature and the soil water content, such that respiration increases as soil water content increases and as soil temperature increases (see Appendix 4 of Vilà-Guerau de Arellano & van Heerwaarden (2015) for the full formulation of soil-respiration used in the model). This is also shown in Figure 4.4 by the "soil respiration feedback" loop and the black closed arrow connecting soil moisture (sm) to soil respiration, which indicates a positive relationship.

The discrepancies between the assimilation and soil respiration rates of the different sensitivities are explained using the feedback loops in Figure 4.4. The case decreasing soil moisture shows reduced assimilation (An), due to an increase in stomatal resistance. The case of reduced moisture in the FT has a similar assimilation magnitude to the control case. The increased potential temperature case has an increase assimilation magnitude compared to the control, which is explained following the "temperature-assimilation feedback" loop (blue feedback loop) in Figure 4.4. For the increased CO_2 concentration case, more CO_2 is available to be taken up by the plant, so the assimilation magnitude is increased (see the "CO_2-assimilation feedback" loop in Figure 4.4). In the reduced soil moisture case, the respiration flux is greater than the control case, as even though soil water content has decreased, the increase in soil temperature (due to more energy being partitioned into sensible heat flux) has a greater impact in determining the soil respiration flux. The other sensitivity cases which have an increased potential temperature compared to the control (increased potential temperature case and increased CO_2 concentration case) have an increased soil temperature and therefore an increased respiration flux, compared to the control. The sensitivity case with reduced moisture in the FT has reduced potential temperature compared to the control case, and therefore shows a decreased respiration flux.
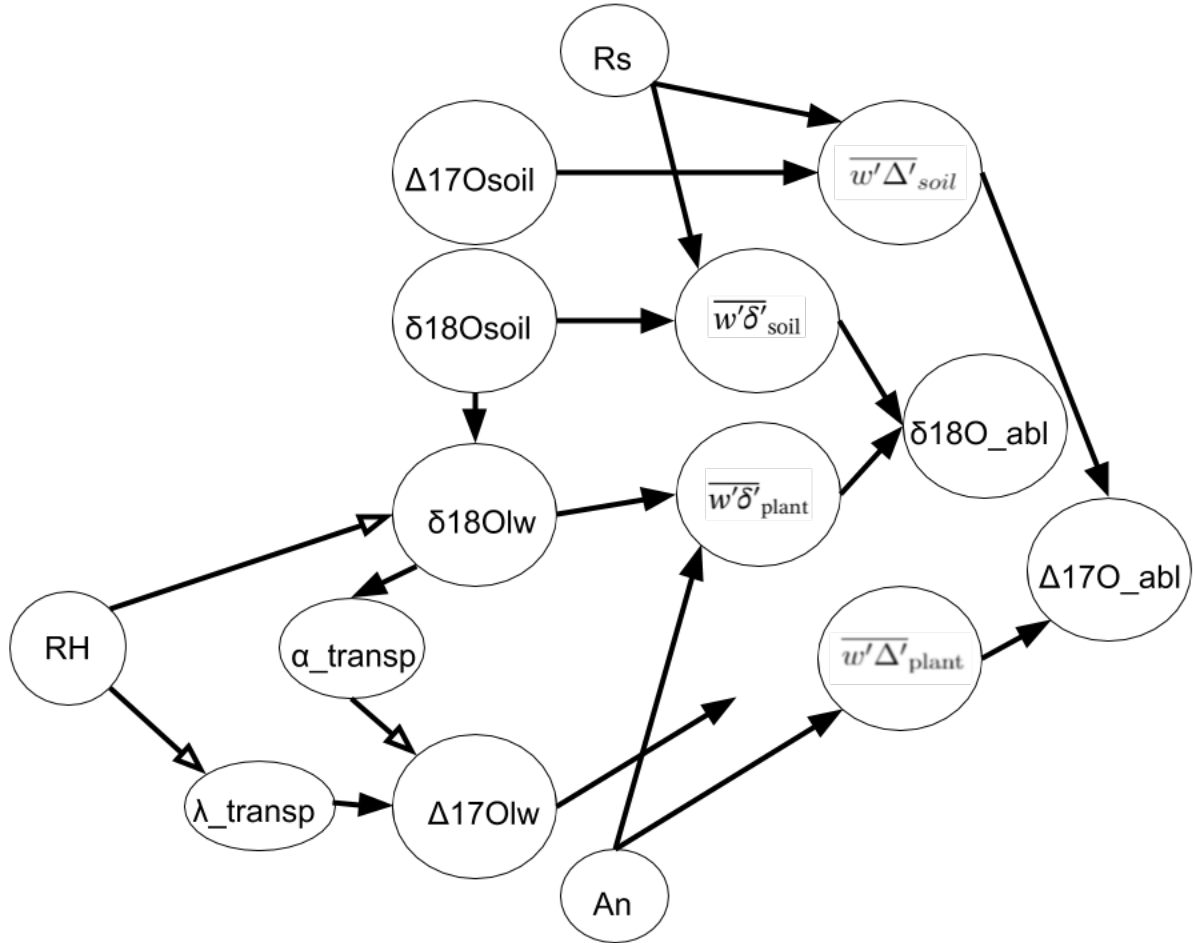
4.2.3 Isotopic signatures

Figure 4.6: Isotope pathways for $\delta^{18}O(CO_2)$ and $\Delta^{17}O(CO_2)$, which describe what factors affect the isotopic signal in the leaf and the soil, and how these isotopic signal can be transferred into the ABL. Closed arrows (black) indicate a positive relationship and open arrows (white) indicate a negative relationship. RH is the relative humidity in the ABL, λ_{transp} is the slope of the line connecting the isotopic composition of leaf water and xylem water in a $\delta^{17}O$ versus $\delta^{18}O$ plot, α_{transp} is the fractionation factor of transpiration of $H_2^{18}O$ relative to $H_2^{16}O$, $\delta^{18}O_{lw}$ and $\Delta^{17}O_{lw}$ are the isotopic compositions of leaf water, $\delta^{18}O_{\text{soil}}$ and $\Delta^{17}O_{\text{soil}}$ are the isotopic compositions of soil water, $\overline{w'\delta'}$ and $\overline{w'\Delta'}$ are the turbulent fluxes of $\delta^{18}O$ and $\Delta^{17}O$ between the soil/plant and the ABL, and $\delta^{18}O_{abl}$ and $\Delta^{17}O_{abl}$ are the isotopic compositions of CO_2 in the ABL.

We consider surface processes from the soil and from the leaf which contribute to the isotopic composition of CO_2 in the ABL. Figure 4.6 illustrates how the isotopic composition within the leaf and the soil influence the isotopic composition of CO_2 in the ABL. The isotopic composition of leaf water and soil water is transferred to CO_2 through isotopic equilibration, which is then transferred to the ABL through an "isoflux". In the MXL model used in this

41

study, the isotopic composition of soil water (which is equal to the isotopic composition of xylem water, $\delta^{18}O_x$) is fixed at $\delta^{18}O_{soil} = 30‰$, whereas the isotopic composition of leaf water is variable, and its evolution is based on enrichment due to evapotranspiration. Relative humidity (RH) is the primary meteorological variable which determines the isotopic composition of leaf water, and, as Figure 4.6 shows, it is negatively related to the $\delta^{18}O$ value of leaf water $\delta^{18}O_{lw}$, so as RH decreases, the leaf water becomes more enriched in ^{18}O. $\Delta^{17}O$ of leaf water is also dependent on RH, but the relationship is more complicated, and will be explained in section 4.2.3.1. Figure 4.6 shows that the two variables which are important to the isoflux are the isotopic composition of the source (leaf water or soil water) and the CO_2 flux from the source into the ABL (assimilation, An, or soil respiration, Rs).

In section 4.2.3.1, the isotopic signatures of leaf water and of CO_2 in equilibrium with leaf water will be explained, then in section 4.2.3.2, the isofluxes between the surface (soil and leaf) and the ABL are discussed, and in section 4.2.3.3, the isotopic signature of ABL CO_2 is examined.

4.2.3.1   Isotopic Signature in the Leaf

To start, the $\delta^{18}O$ signal of leaf water and of CO_2 in equilibrium with leaf water are discussed, then these signals will be used to help explain the corresponding $\Delta^{17}O$ signals.

The $\delta^{18}O$ signal of leaf water is governed by the equation (Gillon & Yarik 2001, Craig & Gordon 1965),

$$\delta^{18}O_{lw} = \delta^{18}O_x + \epsilon_{eq} + \epsilon_k^w + RH(\delta^{18}O_{wv} - \epsilon_k^w - \delta^{18}O_x)\alpha_{eq},$$

(4.1)

where $\delta^{18}O_x = 30‰$ is the isotopic signature of xylem water (the model assumes this to be equal to the signature of the soil water, and so is constant), ϵ_{eq} is the equilibrium fractionation, ϵ_k^w is the canopy-scale kinetic fractionation factor for $H_2^{18}O$, RH is the relative humidity in the ABL, $\delta^{18}O_{wv}$ is isotopic signal of atmospheric water vapour, and α_{eq} is the equilibrium fractionation factor.

The isotopic signature of CO_2 in equilibrium with leaf water is given by (Brenninkmeijer et al. 1983),

$$\delta^{18}O_{CO2\text{-}eq} = \delta^{18}O_{lw} + \frac{17604}{T_c} - 17.93,$$

(4.2)

where T_c is the canopy temperature (which is taken to be the same as the surface temperature).

Figure 4.7 shows the diurnal evolution of $\delta^{18}O$ of leaf water (a) and CO_2 in equilibrium with leaf water (b) for the control case and the four sensitivity analyses. The relations are explained by looking at equation 4.1; RH and $\delta^{18}O_{lw}$ are negatively related, as the value

$(\delta^{18}O_{wv} - \epsilon_k^w - \delta^{18}O_x)$ is negative. Figure 4.3d shows that the RH decreases throughout the day with a slight increase around 14 UTC, resulting in the leaf water to becoming more enriched in ^{18}O throughout the day until approximately 14 UTC, as shown in Figure 4.7a. The isotope pathway diagram (Figure 4.6) shows this negative relationship between RH and $\delta^{18}O_{lw}$. The isotopic composition of CO_2 in equilibrium with leaf water ($\delta^{18}O_{CO2\text{-}eq}$) follows the same diurnal trend as $\delta^{18}O_{lw}$, due to the relationship in equation 4.2, with an increased magnitude due to the equilibrium fractionation between CO_2 and H_2O, as shown in Figure 4.7b.
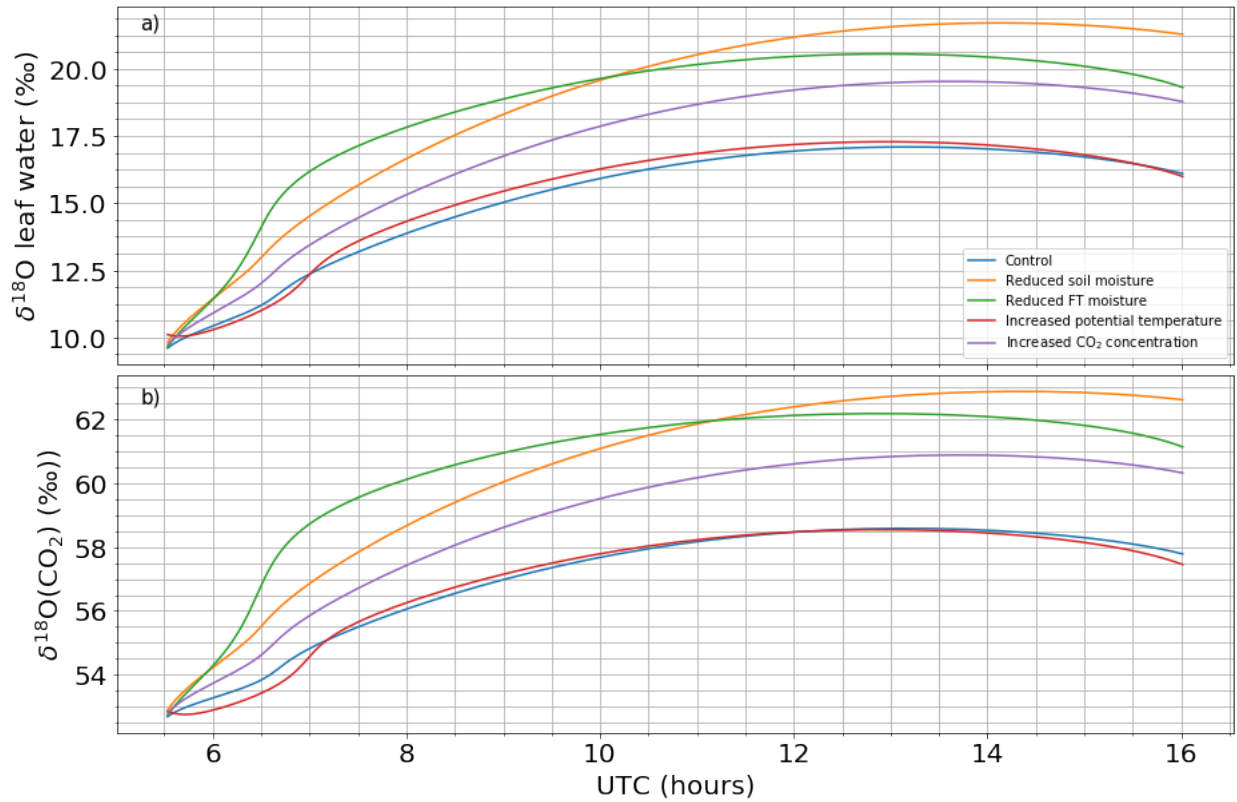

Figure 4.7: a) $\delta^{18}O$ of leaf water and b) $\delta^{18}O$ of CO_2 in equilibrium with leaf water, for the different sensitivity cases. Blue: control, orange: reduced soil moisture, green: reduced FT moisture, red: increased potential temperature, purple: increased CO_2 concentration.

Next, the $\Delta^{17}O$ signals of leaf water and of CO_2 in equilibrium with leaf water are discussed. The equation which the model uses to describe the diurnal evolution of $\Delta^{17}O$ of leaf water is (Koren et al. 2019),

$$\Delta^{17}O_{lw} = \Delta^{17}O_x + (\lambda_{\text{transp}} - \lambda_{\text{RL}})ln(\alpha_{\text{transp}}), \tag{4.3}$$

where, $\Delta^{17}O_x$ is the $\Delta^{17}O$ value of xylem, which is a constant, $\lambda_{\text{RL}} = 0.528$ is the

reference line of mass-dependent fractionation, $\lambda_{\text{transp}} = 0.522 - 0.008RH$ is the slope of the line connecting the isotopic composition of leaf water and xylem water in a $\delta^{17}O$ versus $\delta^{18}O$ plot, as defined by Landais et al. (2006), and $\alpha_{\text{transp}} = \frac{\delta^{18}O_{lw}+1}{\delta^{18}O_{x}+1}$ is the fractionation factor of transpiration of $H_2^{18}O$ relative to $H_2^{16}O$.

In order to investigate how $\Delta^{17}O_{lw}$ evolves throughout the day, we have to investigate how λ_{transp} and α_{transp} vary in equation 4.3. Both parameters depend primarily on RH, λ_{transp} has an negative relationship with RH, which leads to a negative relation of RH with $\Delta^{17}O_{lw}$. α_{transp} has a negative relationship with RH (as $\delta^{18}O_{lw}$ has a negative relationship with RH), however this leads to a positive relation between $\Delta^{17}O_{lw}$ and RH, due to the value of $(\lambda_{\text{transp}} - \lambda_{\text{RL}})$ being negative. Therefore λ_{transp} and α_{transp} have opposing effects on $\Delta^{17}O_{lw}$. This is illustrated in the isotope pathways in Figure 4.6. In order to understand the evolution of the signal throughout the day, we plot the $\Delta^{17}O_{lw}$ signal keeping α_{transp} constant, meaning the evolution of $\Delta^{17}O_{lw}$ is just dependent on λ_{transp}, and the $\Delta^{17}O_{lw}$ signal keeping λ_{transp} constant, so the evolution just depends on α_{transp}. These two trends are shown in Figure 4.8, with green and purple trend lines, respectively, and their analysis allows us to investigate how the two terms interact to make up the resulting $\Delta^{17}O_{lw}$ signal.

Figure 4.8a shows that the full $\Delta^{17}O_{lw}$ signal evolution (blue line) appears to follow the trend which is dependent on α_{transp} (purple line), however the amplitude of the signal is modulated by the λ_{transp} term (green line). The signal depends on the choice of λ_{RL}, as this determines strength of the $ln(\alpha_{\text{transp}})$ term in equation 4.3. For example, changing the reference line to $\lambda_{\text{RL}} = 0.5229$ (the CO_2-water equilibration line), produces the graph in Figure 4.8b. In this case, the amplitude of signal which is only dependent on α_{transp} is about halved compared to the case with $\lambda_{\text{RL}} = 0.528$ (Figure 4.8a). This results in the full $\Delta^{17}O_{lw}$ signal having a smaller magnitude and diurnal variation. The trend is ultimately determined by the interaction between α_{transp} and λ_{transp}, and which of these is signals is more dominant in the relation given in equation 4.3. It is also important to note that the $\Delta^{17}O_{lw}$ trend in the morning is determined by initial conditions of the model. From this analysis, the $\Delta^{17}O$ signal of leaf water is less influenced (has a weaker amplitude) by the external factor RH than the $\delta^{18}O$ signal of leaf water.
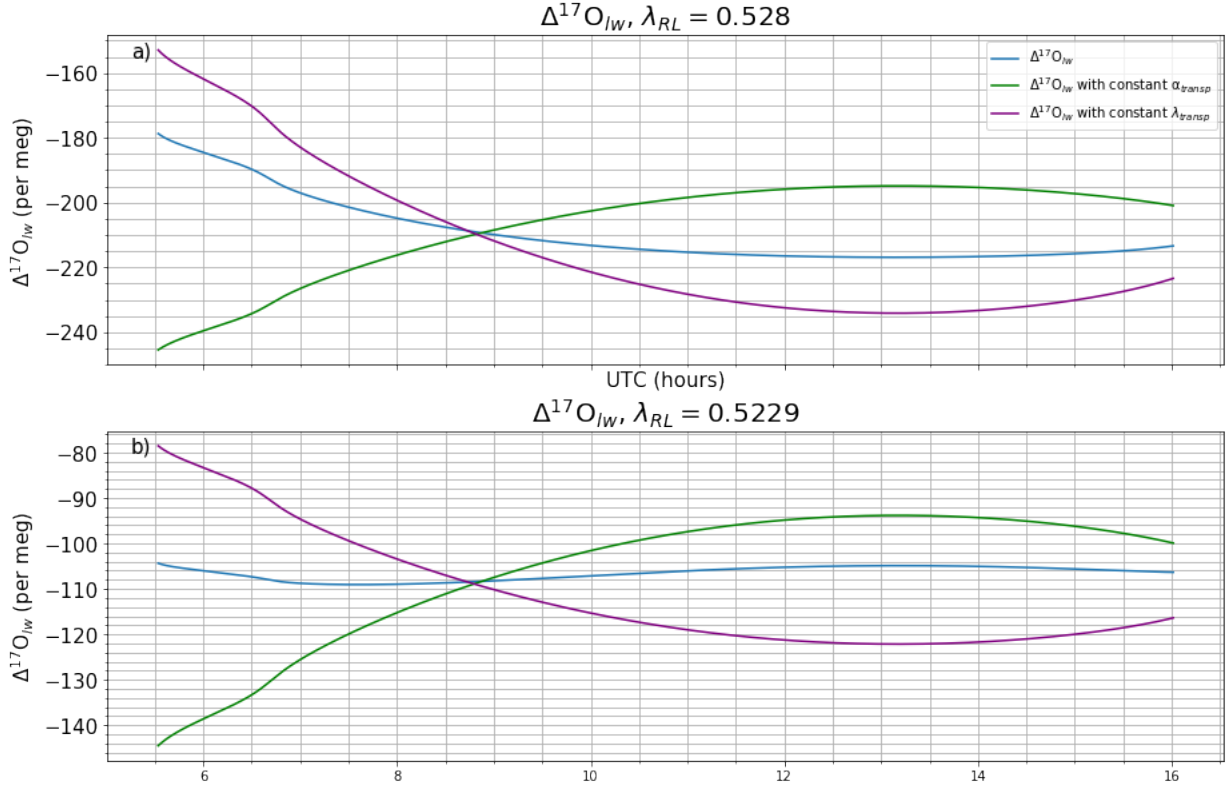
Figure 4.8: $\Delta^{17}O$ of leaf water, with α_{transp} held constant in equation 4.3 (green line), with λ_{transp} held constant in equation 4.3 (purple line), and with both α_{transp} and λ_{transp} varying (blue line). A mass dependent reference line of $\lambda_{\text{RL}} = 0.528$ is used in (a), and a mass dependent reference line of $\lambda_{\text{RL}} = 0.5229$ is used in (b).

The equation used to describe $\Delta^{17}O$ of CO_2 in equilibrium with leaf water, derived by Koren et al. (2019), is,

$$\Delta^{17}O_{\text{CO2-eq}} = \Delta^{17}O_{lw} + (\lambda_{\text{CO2-H2O}} - \lambda_{\text{RL}})ln(\alpha_{\text{CO2-H2O}}) \tag{4.4}$$

where, $\lambda_{\text{CO2-H2O}} = 0.5229$ is the CO_2-H_2O equilibration line (Barkan & Luz 2012), and $\alpha_{\text{CO2-H2O}} = 1 + \frac{17604/T_c - 17.93}{1000}$ is the equilibrium fractionation factor associated with ^{18}O between CO_2 and H_2O, as defined by Brenninkmeijer et al. (1983). The $\Delta^{17}O_{\text{CO2-eq}}$ signal follows the same diurnal evolution as $\Delta^{17}O_{lw}$, with the signal having a different magnitude, due to the last term on the RHS of equation 4.4. The model outputs of $\Delta^{17}O_{lw}$ and $\Delta^{17}O_{\text{CO2-eq}}$ for the different sensitivity analyses are shown in Figure 4.9.
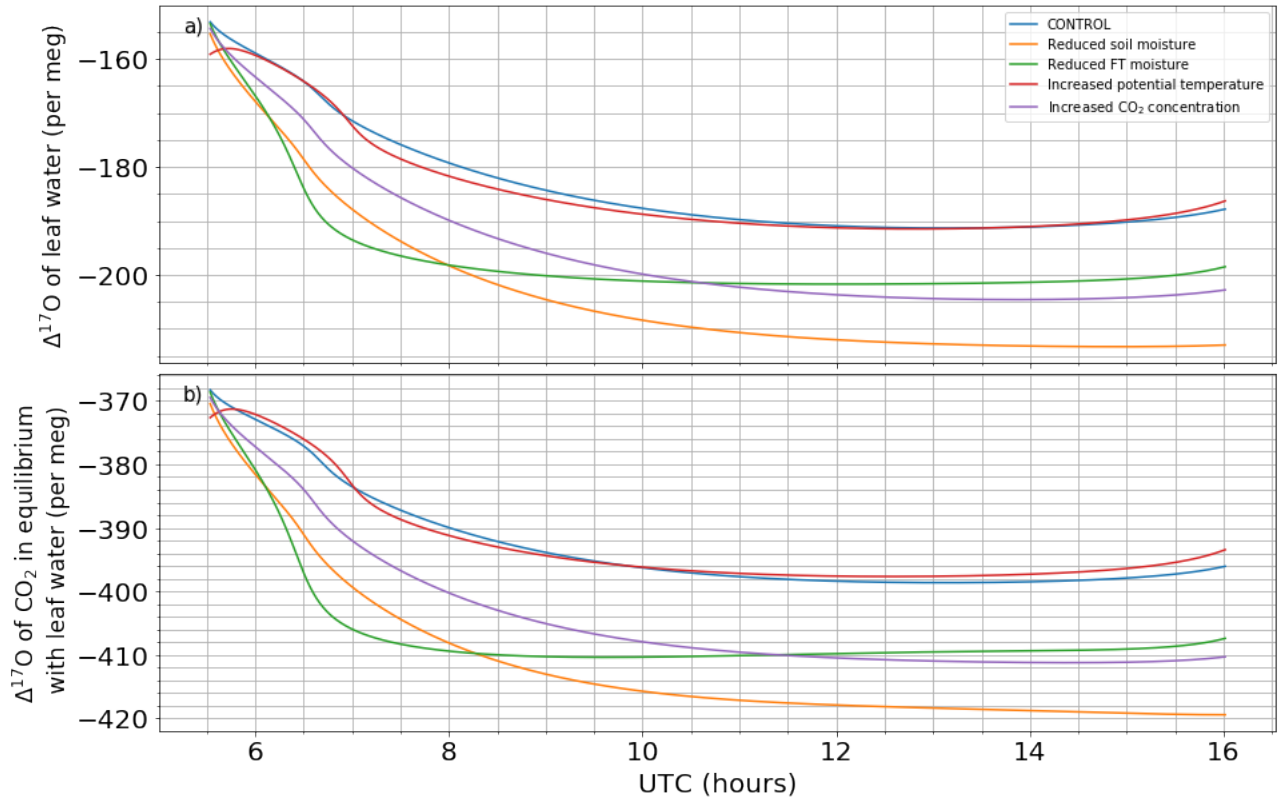
Figure 4.9: a) $\Delta^{17}O$ of leaf water and b) $\Delta^{17}O$ of CO_2 in equilibrium with leaf water, for the control case and the four sensitivity cases. Blue: control, orange: reduced soil moisture, green: reduced FT moisture, red: increased potential temperature, purple: increased CO_2 concentration.

Figure 4.9a shows that the $\Delta^{17}O_{lw}$ signal for all the sensitivity cases are more negative than that of the control case, this is due to a reduced RH in each of the sensitivity cases compared to the control case (see Figure 4.3d). The $\Delta^{17}O_{lw}$ signal follows the trend of relative humidity, due to the trend of of the signal being more strongly influence by the α_{transp} term (Figure 4.8a). Figure 4.9b shows that the $\Delta^{17}O$ signal of CO_2 in equilibrium with leaf water follows the signal of $\Delta^{17}O_{lw}$, with a different magnitude, as CO_2-H_2O equilibration leads to higher $\delta^{18}O$ value of CO_2 in equilibrium with leaf water, but with a three isotope slope that is smaller than the reference slope.

4.2.3.2 Surface Isofluxes

Lee et al. (2009), has shown that the covariance term $\overline{w'\delta'}$ (the turbulent eddy flux of δ), is the same as the ecosystem "isoforcing" on the atmosphere (see equations (3) to (8) in Lee et al. (2009)). Isoforcing is the measure of the isotopic influence of a CO_2 source or sink to the isotopic composition of atmospheric CO_2, and so $\overline{w'\delta'}$ is an appropriate flux to study

46

the land-air isotopic exchange. This is a useful conclusion, as direct measurements of $\overline{w'\delta'}$ can be made with eddy covariance techniques using lasers, and these can be compared to model runs (Griffis et al. 2008).

In this research the turbulent isoflux is defined as the mixing ratio of CO_2 in the atmosphere, $\langle c \rangle$, multiplied by $\overline{w'\delta'}$. The isoflux has dimensions ‰ μmol m^{-2}s^{-1}. The isoflux of an isotopologue from the surface is made up of contributions from the plant and from the soil. The sign convention of the isofluxes is such that a positive (negative) isoflux indicates an enrichment (depletion) of the heavier isotopologue with respect to the more abundant lighter isotopologue in the ABL.

The isotope pathway diagram, Figure 4.6, demonstrates the role that $\overline{w'\delta'}$ plays in the isotopic composition of CO_2 in the ABL. It can be seen from Figure 4.6 that the two variables which influence $\overline{w'\delta'}$ are the isotopic composition of the leaf water or the soil water, and assimilation (An) or respiration (Rs). The model outputs the turbulent eddy fluxes of δ, $\overline{w'\delta'}$, for $CO^{18}O$. The turbulent eddy fluxes of δ consists of contributions from the plant and from the soil,

$$\overline{w'\delta'} = (\overline{w'\delta'})_{\text{plant}} + (\overline{w'\delta'})_{\text{soil}}. \tag{4.5}$$

The plant and soil isofluxes for $CO^{18}O$ are derived in Lee et al., 2009, and are repeated here in equations 4.6 and 4.7, respectively.

$$\overline{w'\delta'}_{\text{plant}} = \frac{\overline{w'c'}_{\text{plant}}}{\langle c \rangle} \left[\frac{c_{\text{cs}}}{c_{\text{cs}} - \langle c \rangle} (\delta_e^{18} - \delta_a^{18})\theta_{\text{eq}} + (1 - \theta_{\text{eq}})\epsilon_k^{18} \frac{c_{\text{cs}}}{\langle c \rangle} - \epsilon_k^{18} \right] \tag{4.6}$$

where, $\overline{w'c'}_{\text{plant}}$ is the turbulent flux of the most abundant CO_2 isotopologue ($CO^{16}O$) into the plant, which is assumed to be equal the assimilation flux (see Figure 4.5a), $\langle c \rangle$ is the concentration of CO_2 in the ABL, c_{cs} is the mixing ratio of CO_2 in the chloroplast, δ_e^{18} is the $\delta^{18}O$ value of CO_2 in equilibrium with leaf water, δ_a^{18} is the $\delta^{18}O$ value of CO_2 in the ABL, θ_{eq} is the degree of oxygen isotope equilibration between CO_2 and H_2O at leaf level and ϵ_k^{18} is the canopy-scale kinetic fractionation factor due to diffusion for $CO^{18}O$.

Figure 4.10a shows that the plant contribution to the $CO^{18}O$ isoflux is always positive, as assimilation causes an increase in the $\delta^{18}O(CO_2)$ value in the ABL, due to back diffusion of more enriched CO_2 from the leaves. The $CO^{18}O$ isoflux from the plant peaks at around midday, as plants become more photosynthetically active causing more stomata to open and more CO_2 to diffuse into the leaf. As more CO_2 diffuses in, more CO_2 will equilibrate with the leaf water and diffuse back from the leaf, increasing the isoflux from the leaf. The isoflux from the plant is greatest for the increased CO_2 concentration case, as this case has the greatest amount of CO_2 diffusing into the stomata (see the assimilation fluxes in Figure 4.5a). The smallest isoflux from the plant is in the reduced soil moisture case, as

with assimilation flux, this is due to less stomata being open, and so less CO_2 entering the choloroplast, equilibrating with leaf water and back diffusing into the ABL. The case with reduced moisture in the FT has an increased $CO^{18}O$ isoflux compared to the control case, despite having the same assimilation flux (Figure 4.5a). This is due to the back-diffused CO_2 from the leaf being more enriched in ^{18}O, as the leaf water in this case is more enriched in ^{18}O compared to the control (see Figure 4.7).

The isoflux of $CO^{18}O$ from soil is described by equation 4.7,

$$\overline{w'\delta'}_{\text{soil}} = \frac{\overline{w'c'}_{\text{soil}}}{\langle c \rangle} \left[\frac{c_{\text{soil}}}{c_{\text{soil}} - \langle c \rangle} (\delta_s^{18} - \delta_a^{18}) - \epsilon_{k,s}^{18} \right] \tag{4.7}$$

where, $\overline{w'c'}_{\text{soil}}$ is the CO_2 flux from soil respiration, c_{soil} is the CO_2 mixing ratio in the soil, $\epsilon_{k,s}^{18}$ is the kinetic fractionation for soil respiration for $CO^{18}O$.

Figure 4.10b shows the soil respiration contribution to the $CO^{18}O$ isoflux is always negative, indicating that respiration is a process which acts to decrease the ^{18}O value in the ABL. The relative amplitudes of the soil isofluxes for the different sensitivity analyses correspond to their respiration flux amplitudes (Figure 4.5b). The case with increased CO_2 concentration has a larger $CO^{18}O$ isoflux magnitude from the soil due to the increased value of $\langle c \rangle$.

Figure 4.10c shows that the increased CO_2 concentration case is the only case to give a positive total $CO^{18}O$ surface isoflux during the day (from 8 UTC to 14:30 UTC), making it the only case where the surface processes can contribute to an increase in the isotopic composition of atmospheric CO_2.

The surface isoforcings corresponding to $\Delta^{17}O(CO_2)$ are derived from the linear definition of $\Delta^{17}O$,

$$\overline{w'\Delta'} = \overline{w'\delta^{17\prime}} - \lambda_{RL}\overline{w'\delta^{18\prime}}. \tag{4.8}$$

As with $CO^{18}O$ isofluxes, the $\Delta^{17}O(CO_2)$ isofluxes from the plant, soil and total surface are defined as $\langle c \rangle \overline{w'\Delta'}$, and are shown in Figure 4.11. The isoflux between the plant and the ABL, shown in Figure 4.11a, is negative, indicating that the back-diffused CO_2 works to decrease the $\Delta^{17}O(CO_2)$ signal in the ABL. The sensitivity case with increased CO_2 concentration in the ABL has the greatest isoflux magnitude, because it has the greatest assimilation flux (Figure 4.5a). The case with reduced soil moisture, on the other hand, has the smallest isoflux magnitude, due to decreased assimilation, as was explained previously in the discussion on $CO^{18}O$ isofluxes. The sensitivity with decreased moisture in the FT has a slightly increased plant isoflux magnitude (more negative) than the control, despite having the same assimilation flux (Figure 4.5a), this is because the CO_2 back-diffused from the leaf has a more negative $\Delta^{17}O$ signal, due to the more negative $\Delta^{17}O$ signature of leaf water and of CO_2 in equilibrium with leaf water (see Figure 4.9).
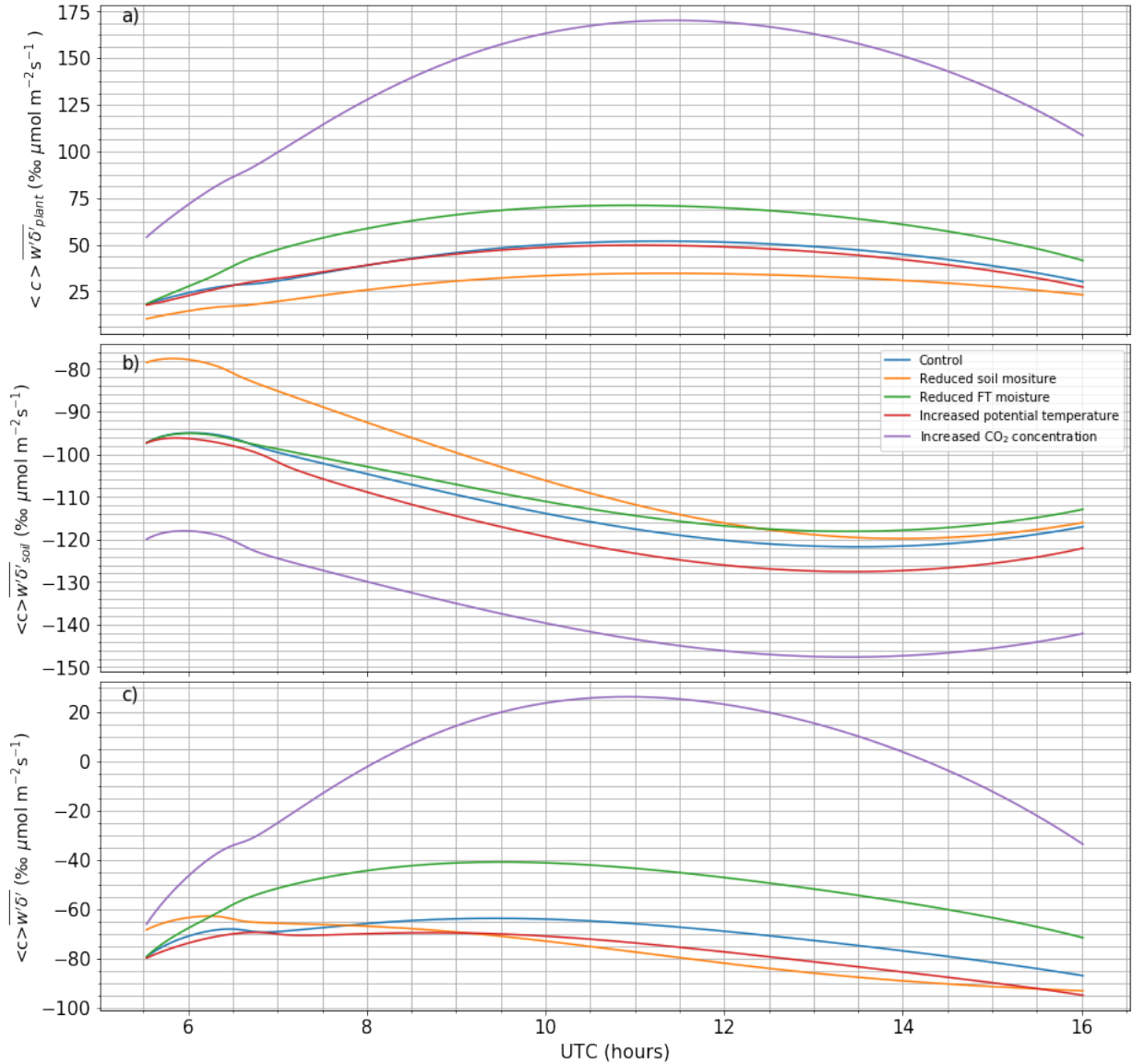
Figure 4.10: Isofluxes of $CO^{18}O$ from a) plant, b) soil, and c) total surface, under the different sensitivity analysis cases, in units ‰μmol m^{-2}s^{-1}. A positive (negative) value of the isoflux indicates that there is an enrichment (depletion) if the heavier isotope with respect to the more abundant lighter isotope in the ABL. Blue: control, orange: reduced soil moisture, green: reduced FT moisture, red: increased potential temperature, purple: increased CO_2 concentration.

The $\Delta^{17}O(CO_2)$ isoflux between the soil and the ABL are shown in Figure 4.11b. The magnitude is positive, which demonstrates that this isoflux works to increase the $\Delta^{17}O(CO_2)$ signal in the ABL. This result is contradictory to the assumption that any isotopic exchange between atmospheric CO_2 and water reservoirs at the earth's surface work to decrease the $\Delta^{17}O$ signature of CO_2 in the ABL. This could be due to the isotopic composition prescribed to the soil, which results in the $\Delta^{17}O$ signal of soil water being greater than that of CO_2 in the ABL. The diurnal trend follows the diurnal soil respiration trend (Figure 4.5b). For the control, reduced FT moisture and increased potential temperature cases, the relative amplitudes of the signals corresponds to the relative amplitudes of the soil respiration fluxes. The amplitude of the soil $\Delta^{17}O(CO_2)$ isoflux corresponding to the sensitivity case with increased CO_2 concentration is larger than the other cases due to a larger value of $\langle c \rangle$.

The total $\Delta^{17}O(CO_2)$ isoflux between the surface and the ABL for each sensitivity case is shown in Figure 4.11c. The isoflux is net negative, so works to decrease the $\Delta^{17}O(CO_2)$ signal in the ABL, with exception of the reduced soil moisture case after 13 UTC. From this graph we can see that the plant isoflux is the more important signal making up the $\Delta^{17}O(CO_2)$ isoflux from the surface.

4.2.3.3 Isotopic Composition of CO_2 in the Atmospheric Boundary Layer

Figure 4.12 shows the diurnal evolution of $\delta^{18}O$ of CO_2 in the ABL. This figure shows us that the $\delta^{18}O(CO_2)$ value increases through the morning regime until a steady state has been reached after approximately 12 UTC. The increasing trend in the morning regime is due to the initial conditions set by the model. All the sensitivity cases start at the same initial value, but evolve to different values in the afternoon. Towards the end of the day the case with increased CO_2 concentration shows the highest value of $\delta^{18}O$ in the ABL, as this case has the most positive isoflux from the surface (Figure 4.10c). The case with increased potential temperature has the lowest value of $\delta^{18}O(CO_2)$ in the ABL, as Figure 4.10c shows that the total isoflux from the surface is more negative than that of the control case, which leads to a greater depletion of ^{18}O in ABL CO_2 from the surface processes, compared to the control case.

However, Figure 4.12 shows that the isotopic composition of CO_2 in the ABL is increased in the reduced soil moisture case compared to the control case. This would not be expected if we only consider contributions from surface processes, as the $CO^{18}O$ isoflux from the surface is mostly more negative than the control case. This implies that there are other processes which are important to contributing to the isotopic composition of atmospheric CO_2. Entrainment also influences the isotopic composition of atmospheric CO_2. In section 4.2.4 the relative contributions of surface processes and entrainment to the $\delta^{18}O(CO_2)$ diurnal budget are investigated.

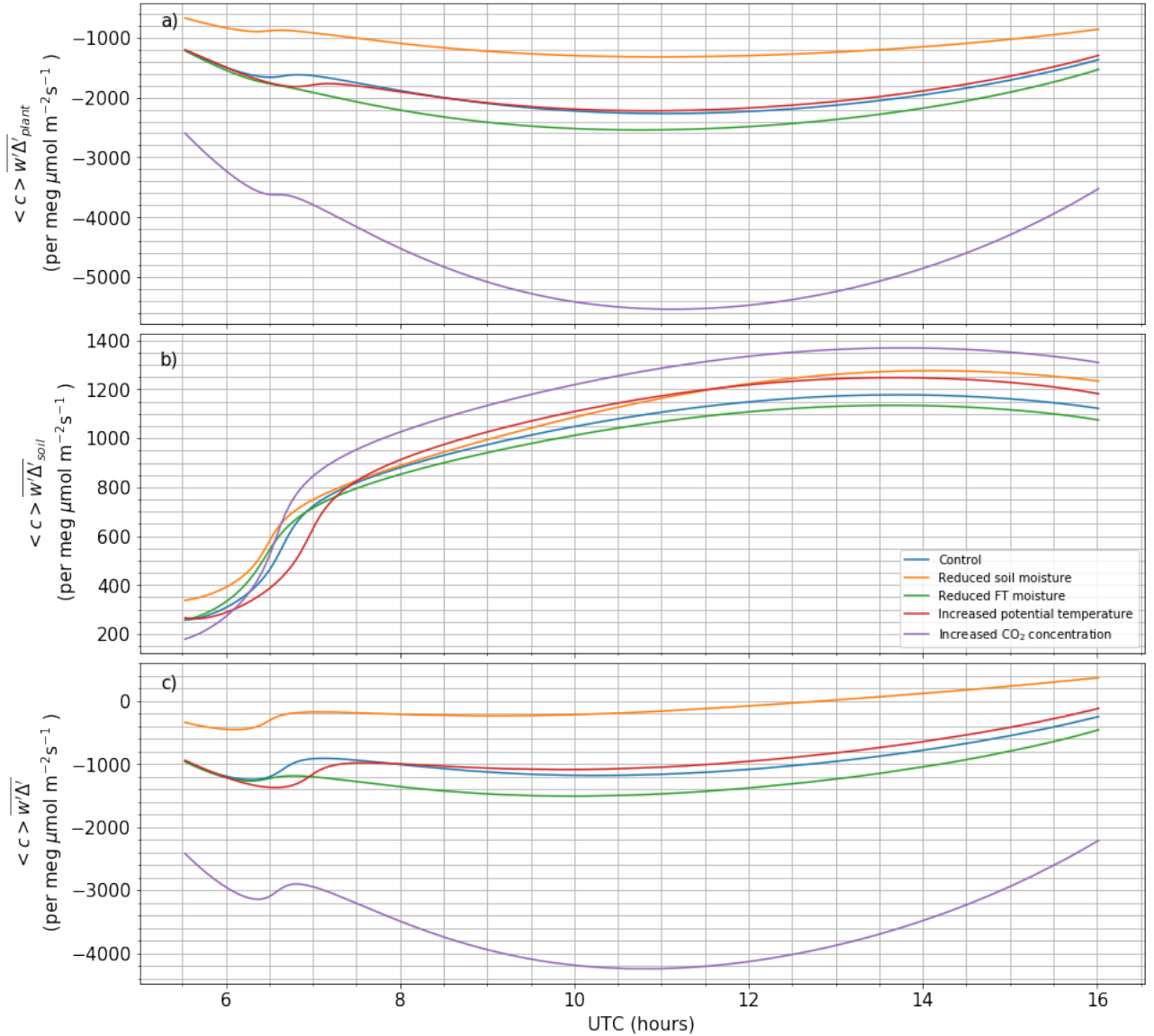Figure 4.11: Isofluxes of $\Delta^{17}O(CO_2)$ from a) plant, b) soil, and c) total surface, under the different sensitivity analysis cases, in units $‰\mu$mol m^{-2}s^{-1}. A positive (negative) value of the isoflux indicates that there is an enrichment (depletion) if the heavier isotope with respect to the more abundant lighter isotope in the ABL. Blue: control, orange: reduced soil moisture, green: reduced FT moisture, red: increased potential temperature, purple: increased CO_2 concentration.
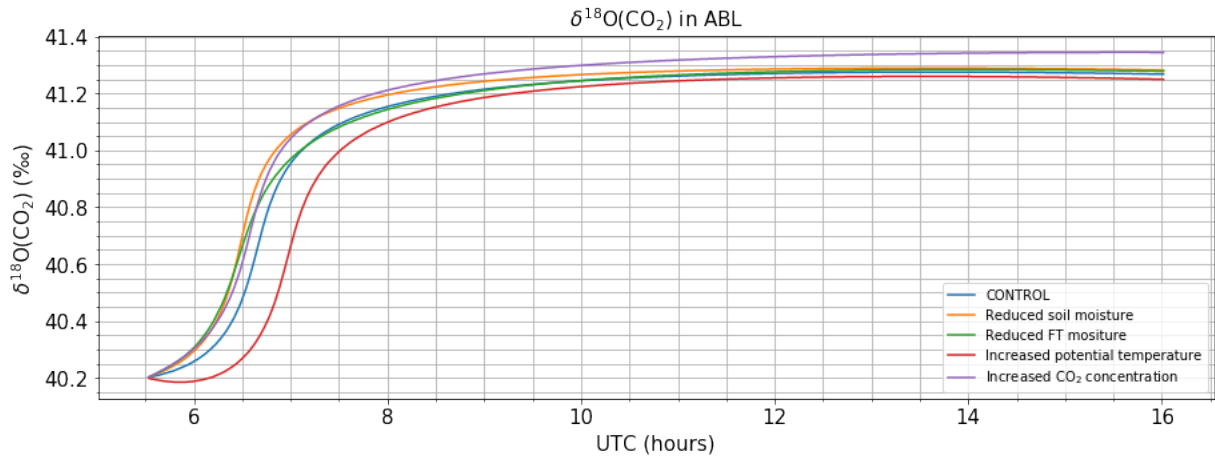
Figure 4.12: $\delta^{18}O(CO_2)$ signal in the ABL, for the control case and the four different sensitivity cases. Blue: control, orange: reduced soil moisture, green: reduced FT moisture, red: increased potential temperature, purple: increased CO_2 concentration.

Figure 4.13 shows the diurnal evolution of the $\Delta^{17}O(CO_2)$ signal in the ABL. The values at the start of the day are due to the initial conditions of the model, and a steady state is reached in the afternoon. The signal is negative and becomes more negative throughout the morning. In section 4.2.4 the relative contributions of the surface processes and entrainment to the $\delta^{18}O(CO_2)$ and $\Delta^{17}O(CO_2)$ diurnal budgets are investigated.

4.2.4 The Isotopic Budgets of CO_2 in the Atmospheric Boundary Layer

The contributions of different sources to the $\delta^{18}O$ value of ABL CO_2 can be investigated by looking at the mass balance equation of $\delta^{18}O(CO_2)$, from equation (7) in Vilà-Guerau de Arellano et al. (2019),

$$\overbrace{\frac{\partial \delta_a^{18}}{\partial t}}^{\text{temporal}} = \overbrace{\frac{\overline{w'\delta'}}{h}}^{\text{surface}} + \overbrace{\frac{1}{h}\frac{\partial h}{\partial t}\frac{c^{FT}}{\langle c \rangle}\left(\delta_{FT}^{18} - \delta_a^{18}\right)}^{\text{entrainment}}. \tag{4.9}$$

The first term on the right hand side of equation 4.9 represents the contribution to $\delta^{18}O(CO_2)$ in the ABL from soil and plant processes. The second term represents the contribution from entrainment to the $\delta^{18}O(CO_2)$ budget. It is assumed that these two processes are the only ones which contribute to the atmospheric $\delta^{18}O$ signal.

Figure 4.14 shows the individual contributions of the plant, soil, total surface and entrainment to the total $\delta^{18}O(CO_2)$ budget for the control case and each of the different sensitivity analyses. The initial morning values for each contribution are due to the initial conditions of the model, and the contributions go to zero in the afternoon as the isotopic
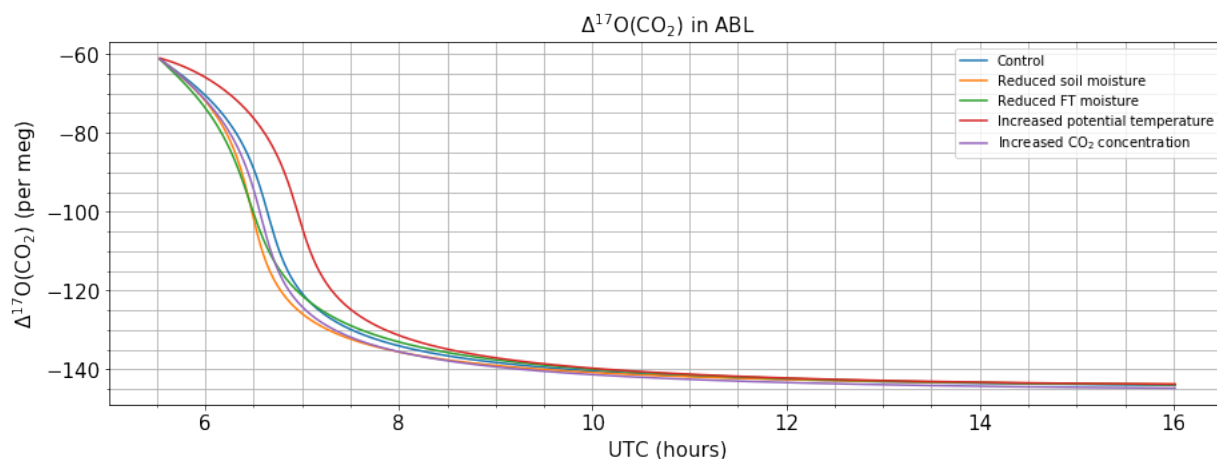
Figure 4.13: $\Delta^{17}O(CO_2)$ signal in the ABL, for the sensitivity cases noted in the legend.

signal in the ABL reaches a steady state (see Figure 4.12). Figure 4.14 shows that the contribution from entrainment is dominant in the morning regime, due to the large entrainment event occurring at approximately 6:30 UTC, in each of the sensitivity cases. The entrainment peak works to increase the $\delta^{18}O$ signal in the ABL, as it corresponds to a positive $\frac{\partial \delta_a^{18}}{\partial t}$ value. The magnitude of the entrainment peak corresponds to the rate of growth of the ABL ($\frac{\partial h}{\partial t}$), therefore, the entrainment peak in the reduced soil moisture case (Figure 4.14b) has the largest magnitude, as the rate of growth of the ABL at approximately 6:30 UTC is the greatest of the sensitivity cases (see Figure 4.3b for the diurnal evolution of the ABL height), while the case with reduced moisture in the FT has the smallest entrainment peak magnitude, corresponding to the smallest ABL growth rate. As the entrainment term dominates over the surface terms in this morning regime, the surface terms are shown in Appendix B individually.

The $\Delta^{17}O(CO_2)$ budget in the ABL is calculated using the linear definition of $\Delta^{17}O$ and the ABL budgets of $\delta^{17}O(CO_2)$ and $\delta^{18}O(CO_2)$,

$$\frac{\partial \Delta_a^{17}}{\partial t} = \frac{\partial \delta_a^{17}}{\partial t} - \lambda_{RL} \frac{\partial \delta_a^{18}}{\partial t}. \tag{4.10}$$

The results for each of the sensitivity analyses are plotted in Figure 4.15. The analysis of this budget is much the same as the analysis for the ABL $\delta^{18}O(CO_2)$ budget. The contribution from entrainment dominates in the morning regime due to the entrainment event occurring at approximately 6:30 UTC. The relative magnitudes of the entrainment peaks for each of the sensitivities are explained by the corresponding growth rate of the ABL, similar to the explanation for the $\delta^{18}O(CO_2)$ budget. The morning contribution for entrainment is negative, meaning that entrainment works to decrease the $\Delta^{17}O(CO_2)$ signal in the ABL. However, we would expect the contribution from the plant to be the

(a) Control

(b) Reduced Soil Moisture

(c) Reduced FT Moisture

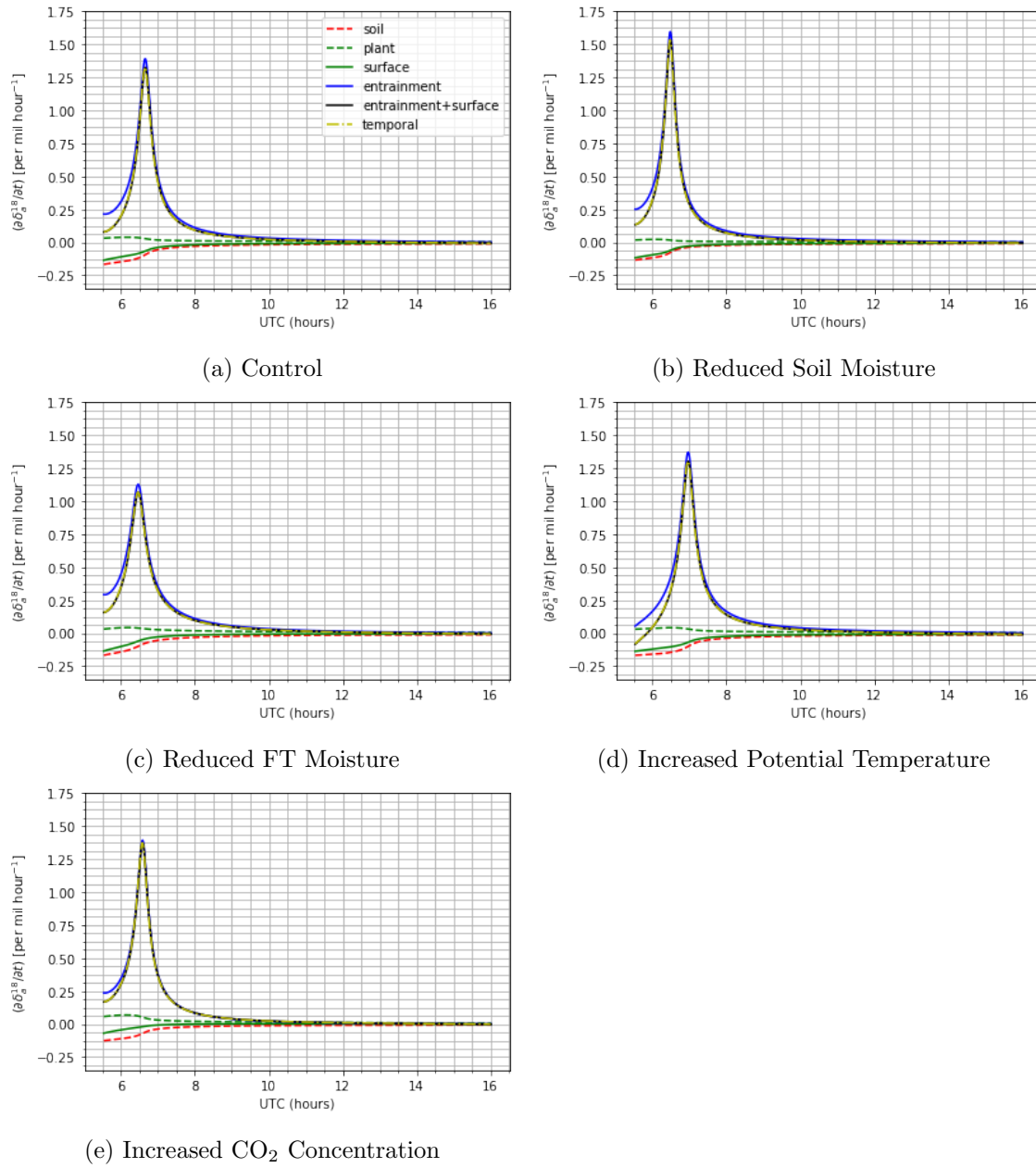(d) Increased Potential Temperature

(e) Increased CO_2 Concentration

Figure 4.14: Diurnal evolution of the separate contributions to the budget of $\delta^{18}O(CO_2)$ for the different sensitivity analyses: a) control case, b) decrease in soil moisture, c) decreased moisture in the free troposphere, d) increase in the initial potential temperature of the ABL, and e) increase in the CO_2 concentration in the ABL. The different contributions to the $\delta^{18}O$ budget are highlighted in the legend in 4.14a.

main process working to decrease the $\Delta^{17}O(CO_2)$ ABL signal, and that the stratospheric signal is larger in the FT compared to the ABL. The $\Delta^{17}O(CO_2)$ signal from entrainment in this model is negative due to the $\Delta^{17}O(CO_2)$ signal in the FT being more negative than the ABL signal, so air with a more negative $\Delta^{17}O(CO_2)$ signal is being entrained into the ABL. The FT was prescribed this isotopic signal in the model in order to correctly recreate the ABL isotopic composition corresponding to the measurements, however, measurements of the isotopic composition of FT CO_2 have not been carried out, so it is not clear whether the isotopic composition of the FT used in this model is accurate. A close up view of the diurnal evolution of the surface contributions can be found in Appendix B.

4.2.4.1   The Afternoon Budget

The isotopic budgets in the ABL comes close to a steady state in the afternoon. In order to study the afternoon regime, the averages from each contribution between 12 UTC and 16 UTC are taken. The results for the afternoon $\delta^{18}O(CO_2)$ and $\Delta^{17}O(CO_2)$ budgets are shown in Figures 4.16 and 4.17, respectively.

Figure 4.16 shows that, across the sensitivity cases, the soil contribution is negative as well as the largest contribution to the $\delta^{18}O(CO_2)$ budget, the plant and entrainment contributions are positive. Therefore, the soil works to decrease the $\delta^{18}O(CO_2)$ value in the ABL, while the plant and entrainment contributions work to increase the $\delta^{18}O(CO_2)$ value in the ABL. The discrepancies between the surface contributions of different sensitivity cases, shown in Figure 4.16, can be explained by referring back to the surface $CO^{18}O$ isoflux graphs (Figure 4.10), as the differences between the isofluxes from the soil/plant of the different sensitivity analyses gives an indication of their respective contributions to the $\delta^{18}O(CO_2)$ budget. The case with reduced soil moisture (Figure 4.16b) has reduced contributions from the soil and the plant, due to smaller isoflux magnitudes, which is explained due to reduced plant activity in this sensitivity case. The case with reduced moisture in the FT (Figure 4.16c) has an increased (more positive) contribution from the plant, due to an increased $CO^{18}O$ isoflux from the plant (Figure 4.10a). This is explained by the back-diffused CO_2 from the leaf in this case being more enriched in ^{18}O than the control case (see Figure 4.7). The increased potential temperature case (Figure 4.16d) has a similar plant contribution to the control case, but the soil contribution is greater (more negative), due to a more negative $CO^{18}O$ soil isoflux (Figure 4.10b), resulting from a greater respiration magnitude (Figure 4.5b). The sensitivity case with increased CO_2 concentration (Figure 4.16e) has an increased contribution to the budget from the plant, due to increased assimilation (Figure 4.5a) leading to a greater isoflux (Figure 4.10a). However, for the increased CO_2 case, the contribution from the soil has decreased compared to the control case, as the soil respiration flux doesn't impact the isotopic composition of ABL CO_2 to the same degree as the control
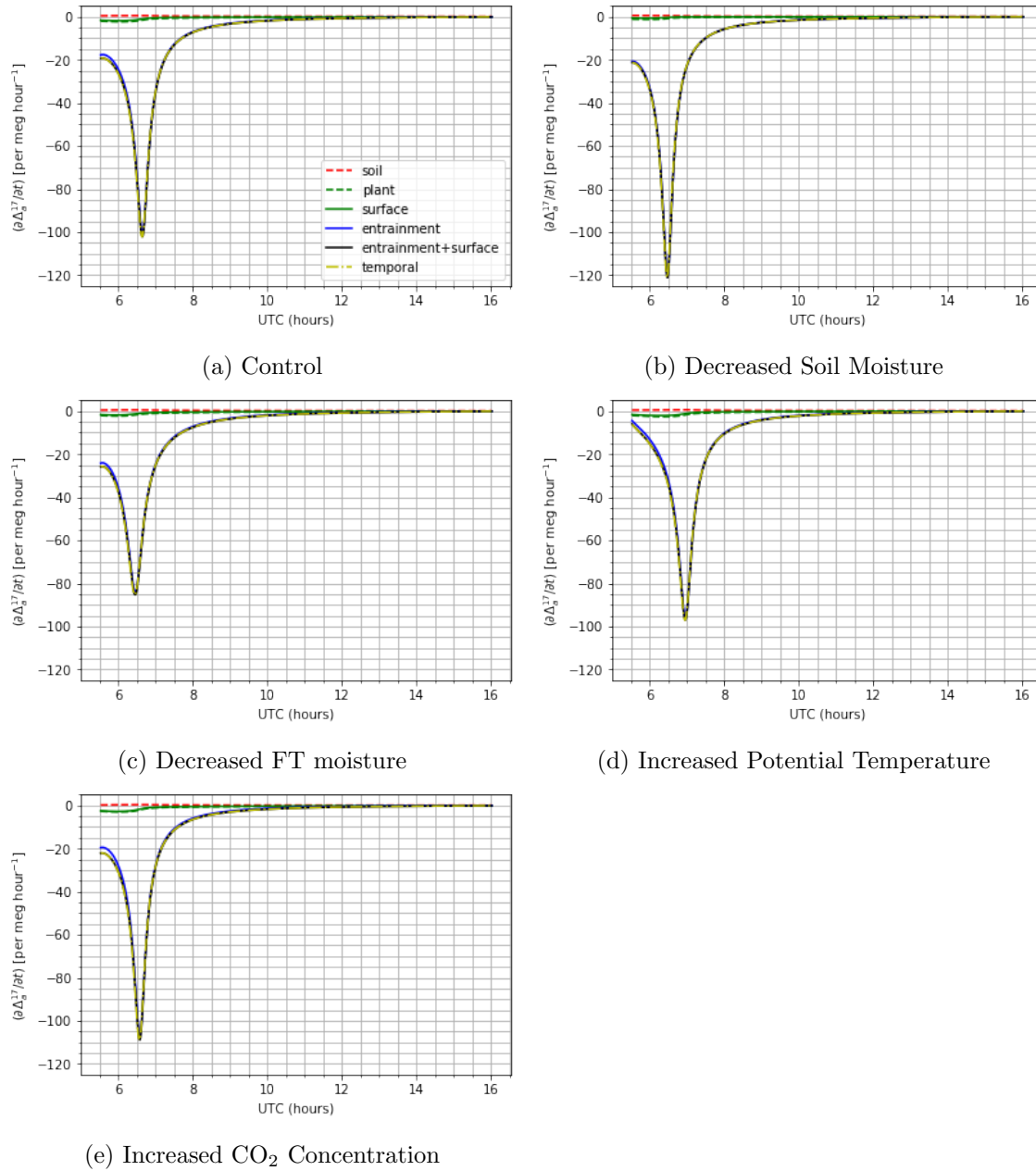
(a) Control

(b) Decreased Soil Moisture

(c) Decreased FT moisture

(d) Increased Potential Temperature

(e) Increased CO_2 Concentration

Figure 4.15: Diurnal evolution of the separate contributions to the budget of $\Delta^{17}O(CO_2)$ for the different sensitivity analyses: a) control case, b) decrease in soil moisture, c) decreased moisture in the free troposphere, d) increase in the initial potential temperature of the ABL, and e) increase in the CO_2 concentration in the ABL. The different contributions to the $\Delta^{17}O$ budget are highlighted in the legend in 4.15a.

case due to increased CO_2 concentration in the ABL.

The information in Figure 4.16 also demonstrates how the entrainment contribution in the afternoon varies under different conditions. Most notably, the entrainment contribution for the increased CO_2 concentration is reduced compared to the control case. This is because the CO_2 in the ABL is more enriched in ^{18}O in the afternoon steady state regime compared to the control case (see Figure 4.12), so the $\delta^{18}O(CO_2)$ gradient between the FT and the ABL is decreased, therefore diminishing the strength of the entrainment contribution to the $\delta^{18}O(CO_2)$ ABL budget. The increased CO_2 concentration case (Figure 4.16e) is the only case to have a positive total contribution from the surface and entrainment (black bars in Figure 4.16), meaning that this is the only case which has an increasing $\delta^{18}O(CO_2)$ ABL signal in the afternoon. The case with reduced moisture in the FT has a total contribution to the budget of zero (Figure 4.16c), meaning that the $\delta^{18}O(CO_2)$ signal in the ABL is constant, not increasing or decreasing.

Figure 4.17 shows that the largest contribution to the $\Delta^{17}O(CO_2)$ afternoon budget regime is entrainment, for all the sensitivity cases, with the exception of the increased CO_2 concentration case, which has the largest contribution from the plant (Figure 4.17e). The surface $\Delta^{17}O(CO_2)$ isofluxes are used to explain the discrepancies between the soil and plant contributions to the afternoon budget of the different sensitivity analyses, as with the $\delta^{18}O(CO_2)$ budget analysis. The case with reduced soil moisture (Figure 4.17b) has reduced contribution from the plant compared to the control, due to a less negative plant $\Delta^{17}O(CO_2)$ isoflux for this case (Figure 4.11a), due to reduced assimilation. The case with reduced moisture in the FT (Figure 4.17c) has an increased contribution from the plant compared to the control, this can be attributed to a more negative $\Delta^{17}O(CO_2)$ isoflux from the plant for this sensitivity, due to CO_2 in equilibrium with leaf water having a more negative $\Delta^{17}O$ signature (Figure 4.9). The increased potential temperature case (Figure 4.17d) has very similar soil and plant contributions to the control. The increased CO_2 concentration case (Figure 4.17e) has an increased contribution from the plant, due to the more negative isoflux (Figure 4.11a), which results from increased assimilation (Figure 4.5a). The soil contribution for this case is decreased compared to the control, which is due to the CO_2 flux from the soil having a smaller impact on the isotopic composition of the ABL, due to the increased CO_2 concentration in the ABL.

The most important thing to note is that the plant contribution is more variable between the different sensitivities compared to the soil or entrainment contributions in Figure 4.17, which indicates that the plant contribution to the $\Delta^{17}O(CO_2)$ budget in the ABL is more sensitive to changes in the meteorology. The increased CO_2 concentration case can be considered an exception, as the soil and entrainment contributions have reduced impact on the isotopic composition of CO_2 in the ABL, as the ABL has a greater concentration of CO_2.
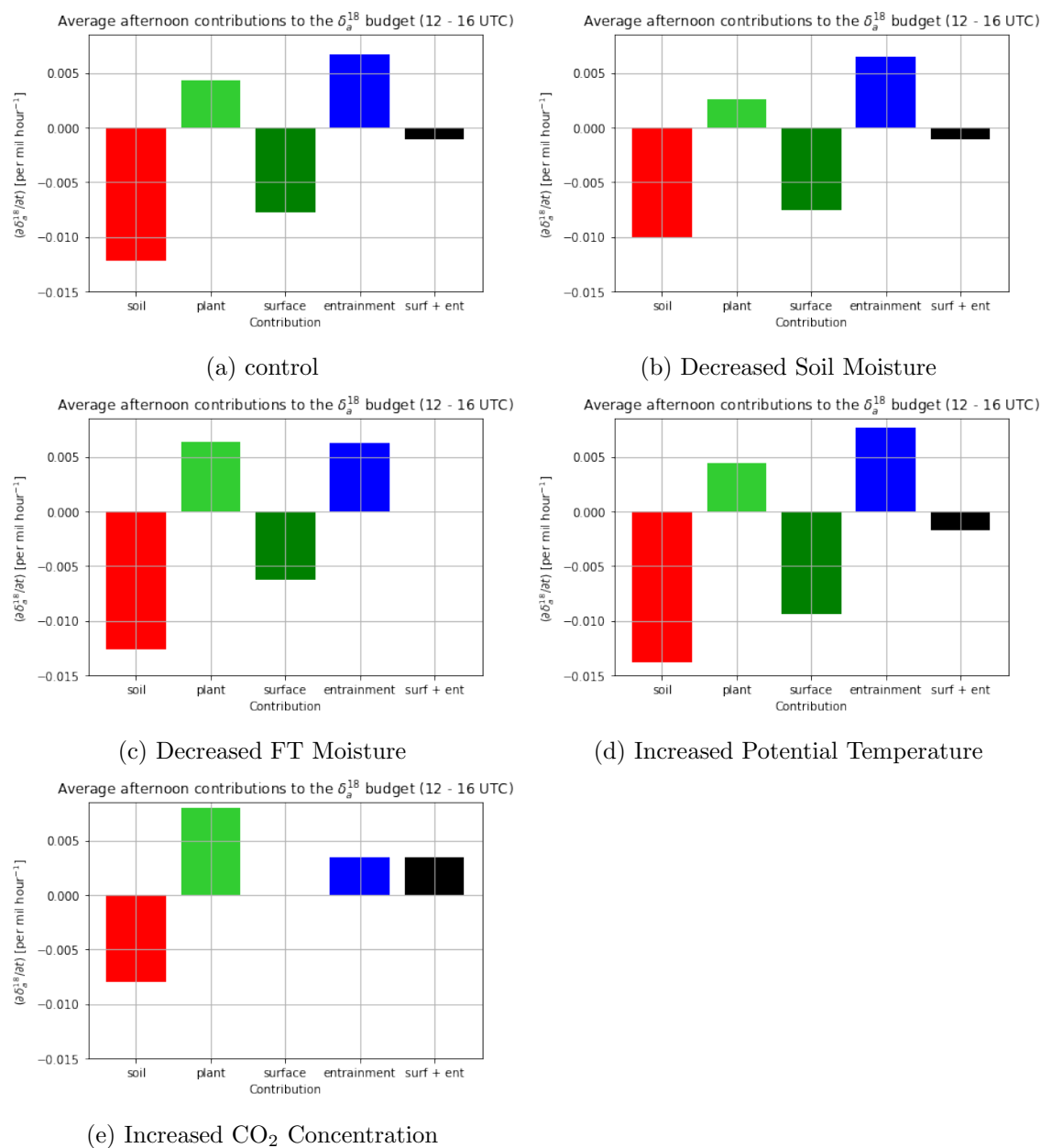
(a) control

(b) Decreased Soil Moisture

(c) Decreased FT Moisture

(d) Increased Potential Temperature

(e) Increased CO_2 Concentration

Figure 4.16: Average afternoon steady state contributions to the $\delta^{18}O(CO_2)$ budget in the ABL under different sensitivity analyses: a) control case, b) decrease in soil moisture, c) decreased moisture in the free troposphere, d) increase in the initial potential temperature of the ABL, and e) increase in the CO_2 concentration in the ABL. The different contributions to the $\delta^{18}O$ budget are highlighted in the legend in 4.14a.

58

This variability in the plant contribution, but not the soil contribution is contrasting to the $\delta^{18}O(CO_2)$ budget (Figure 4.16), which shows a similar degree of variability in both the soil and the plant contributions across the sensitivity analyses. Therefore the soil and plant contributions to the $\delta^{18}O(CO_2)$ signal in the ABL are sensitive to changes in meteorological variables, whereas, the plant contribution is the most sensitive to changes in meteorological variables in the $\Delta^{17}O(CO_2)$ ABL signal.

(a) control

(b) Reduced Soil Moisture

(c) Reduced FT Moisture

(d) Increased Potential Temperature

(e) Increased CO_2 Concentration
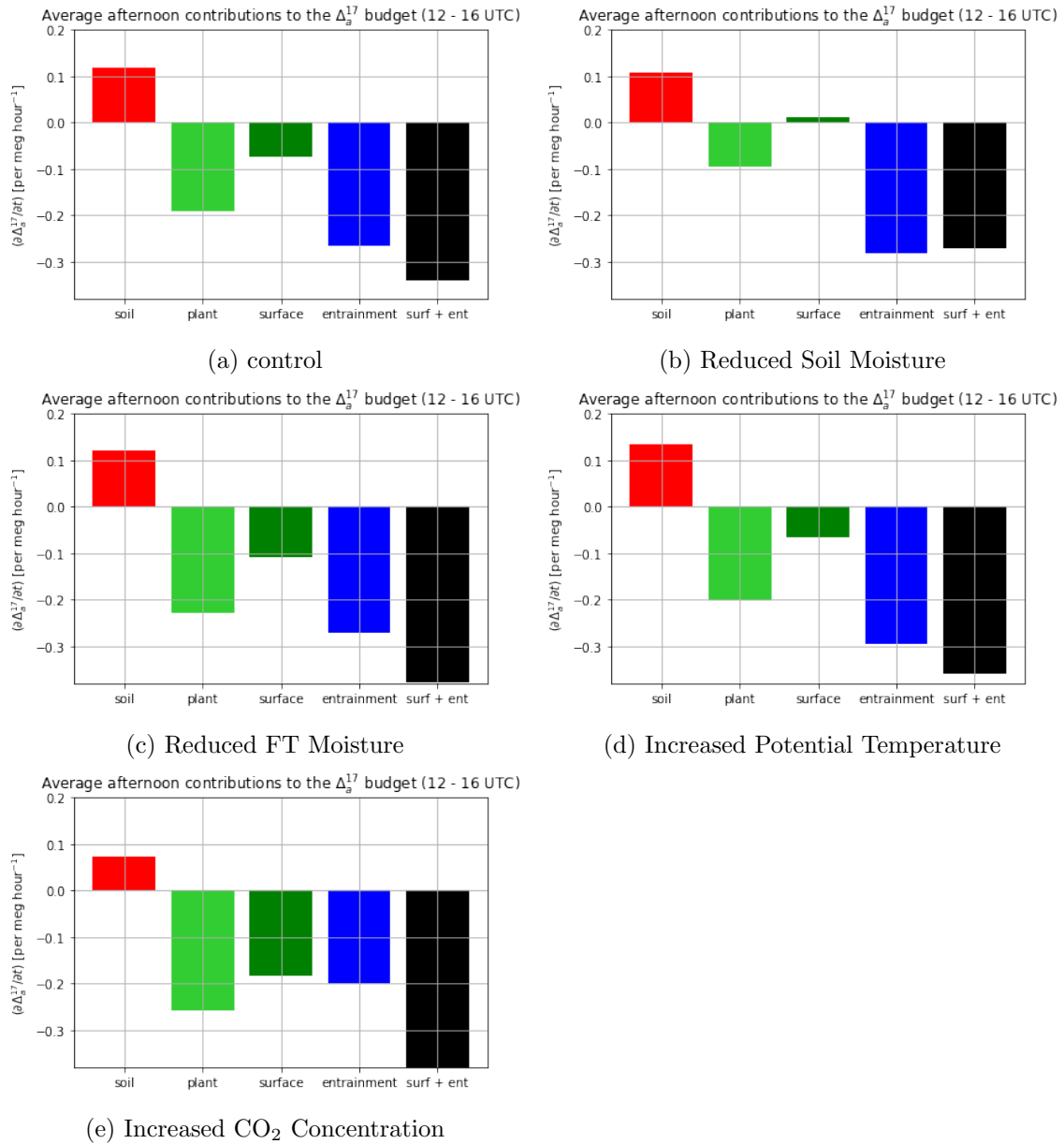
Figure 4.17: Average afternoon steady state contributions to the $\Delta^{17}O(CO_2)$ budget in the ABL under different sensitivity analyses: a) control case, b) decrease in soil moisture, c) decreased moisture in the free troposphere, d) increase in the initial potential temperature of the ABL, and e) increase in the CO_2 concentration in the ABL. The different contributions to the $\Delta^{17}O$ budget are highlighted in the legend in 4.17a.

4.3   Conclusion

This study has investigated how a mixed-layer model has simulated the $\Delta^{17}O(CO_2)$ signal in the ABL above a forest ecosystem, and how this signal changes in response to different initial conditions in the atmosphere. The signal has been studied by investigating how the CO_2 fluxes associated with the soil and the plant impact the isotopic signal in the ABL, as well as investigating how entrainment contributes to the ABL isotopic signal.

Studies of the budgets of $\delta^{18}O(CO_2)$ and $\Delta^{17}O(CO_2)$ in the ABL during the afternoon, steady state regime highlight that the plant contribution to the $\Delta^{17}O(CO_2)$ afternoon signal in the ABL is sensitive to changes in meteorological conditions, while the contributions from the soil and entrainment remain relatively constant. This is contrasting to the $\delta^{18}O(CO_2)$ signal in the ABL, where the soil and plant contributions are both approximately equally sensitive to changes in the meteorology. This suggests that the $\Delta^{17}O(CO_2)$ signal in the ABL is potentially a more appropriate indicator of GPP than $\delta^{18}O(CO_2)$ as changes in its signal are mainly determined by changes in the contribution from the plant, with the soil contribution being less important. Further sensitivity analyses would need to be carried out to investigate how well this hypothesis holds up.

However, Figure 4.17 shows that the changes in the afternoon budget are approximately 0.3 to 0.4 per meg per hour. The precision which can be obtained on the $\Delta^{17}O(CO_2)$ measurement system, calculated in this study (section 3.3.1.1) is in the order of 10 times this signal (10 per meg). Therefore, by this analysis, it is not possible to measure the modelled changes in the afternoon signal. This could potentially limit the effectiveness of $\Delta^{17}O(CO_2)$ as a tracer of GPP, as the GPP changes would need to be much greater than the changes between the sensitivities in this study, in order for any change in GPP to be detected in the afternoon regime. However, this is a mixed layer model and larger variations of $\Delta^{17}O$ could exist in reality, for example within the canopy. The GPP problem is of interest on a much larger scale (continental or global), on the local scale, parameters like entrainment play a more important role.

This study can help to indicate further measurements of $\Delta^{17}O(CO_2)$ which would be interesting to carry out. The contributions from entrainment and the soil contradict the expectation that entrainment would work to increase the $\Delta^{17}O(CO_2)$ signal in the ABL, while the soil would work to decrease the $\Delta^{17}O(CO_2)$ signal in the ABL. In order to verify the entrainment contribution to the $\Delta^{17}O(CO_2)$ ABL budget, measurements of $\Delta^{17}O(CO_2)$ in the FT are necessary, and to verify the soil contributions, measurements of the isotopic composition of soil water are necessary. Measurements of the vertical forest profile could be taken as in this study we have just investigated the signal in the mixed atmospheric layer, above the forest canopy. Taking measurements of the vertical forest profile would allow us to see if the signal is more dominated by soil (a more positive signal) at the floor,

and then becomes more dominated by leaves (a more negative signal), then entrainment as we travel towards the canopy. Also, adding the $\Delta^{17}O(CO_2)$ signal into a two-dimensional in space mixed layer model, would allow the vertical profile of the forest to be modelled, and then the $\Delta^{17}O(CO_2)$ budget may be less dominated by entrainment, allowing better investigation into the roles of the surface processes to the total $\Delta^{17}O(CO_2)$ signal.

Acknowledgements

MXL model sensitivity settings

Due to the set up of the MXL model, the initial concentrations of the isotopologues of CO_2 and H_2O need to be directly input into the model. Therefore, changing certain initial meteorological parameters requires also changing the initial concentrations of theses isotopologues in order to keep the initial δ values of CO_2 and H_2O the same as in the control case. These changes for the relevant sensitivity cases are explained in the following paragraphs.

For Sensitivity 1_1, decreasing the water content in the FT also requires us to decrease the concentration of $H_2^{18}O$ in the FT in order to keep the initial $\delta^{18}O(H_2O)$ (= - 4.9978‰) in the FT constant and to prevent highly enriched H_2O being entrained from the FT into the ABL. In the control case the initial concentration of H_2O in the FT is 14323107.20 ppb and the initial concentration of $H_2^{18}O$ is 28577.15 ppb. The decrease of humidity in the FT results in a new concentration of H_2O in the FT of 9494427.73 ppb. To maintain a $\delta^{18}O(H_2O)$ value of - 4.9978‰, the concentration of $H_2^{18}O$ in the FT is reduced to 18943.07 ppb.

In sensitivity 2, the initial specific humidity in the ABL has to be decreased so that the relative humidity in each sensitivity case has the same initial value, and the magnitude of the specific humidity inversion at the boundary of the ABL and the FT has to be increased, in order to keep to water content in the FT the same. The initial specific humidity in the ABL was changed from 9.0 g/kg to 9.92 g/kg, and the specific humidity inversion was changed from -0.1 g/kg to -1.02 g/kg. The concentration of $H_2^{18}O$ in the ABL has to be increased, so that the initial $\delta^{18}O(H_2O)$ value in the ABL remains constant, the concentration is increased from 28900.09539 ppb to 31855.90730 ppb, as the H_2O concentration is increased from 1.45E+07 ppb to 1.60E+07 ppb.

For Sensitivity 3, the concentration of $CO^{18}O$ and $CO^{17}O$ in the ABL and FT was increased in order to maintain the initial $\delta^{18}O(CO_2)$ and $\delta^{17}O(CO_2)$ values in the ABL and the FT. The values in the FT are $\delta^{18}O(CO_2) = 41.400‰$ and $\delta^{17}O(CO_2) = 21.500‰$, and in the ABL are $\delta^{18}O(CO_2) = 40.200‰$ and $\delta^{17}O(CO_2) = 20.966‰$. For the control case, the initial concentrations in the FT are $[CO^{18}O] = 1754.10$ ppb and $[CO^{17}O] = 325.98$ ppb and the initial concentrations in the ABL are $[CO^{18}O] = 1918.94$ ppb and $[CO^{17}O]$

= 356.84 ppb. Therefore, to maintain constant $\delta^{18}O$ and $\delta^{17}O$ values for CO2 in the FT and ABL, the new concentrations in the FT are $[CO^{18}O] = 3007.030$ ppb and $[CO^{17}O] = 558.907$ ppb, and in the ABL are $[CO^{18}O] = 3128.714$ ppb and $[CO^{17}O] = 581.797$ ppb.

Surface contribution to the isotopic budgets of ABL CO$_2$

(a) control

(b) Reduced Soil Moisture

(c) Reduced FT Moisture

(d) Increased Potential temperature

(e) Increased CO$_2$ Concentration

Figure B.1: Diurnal evolution of the surface contributions to the budget of δ^{18}O(CO$_2$) for the different sensitivity analyses: a) control case, b) decrease in soil moisture, c) decreased moisture in the free troposphere, d) increase in the initial potential temperature of the ABL, and e) increase in the CO$_2$ concentration in the ABL. The different contributions to the δ^{18}O budget are highlighted in the legend in 4.14a.

(a) control

(b) Reduced Soil Moisture

(c) Reduced FT Moisture

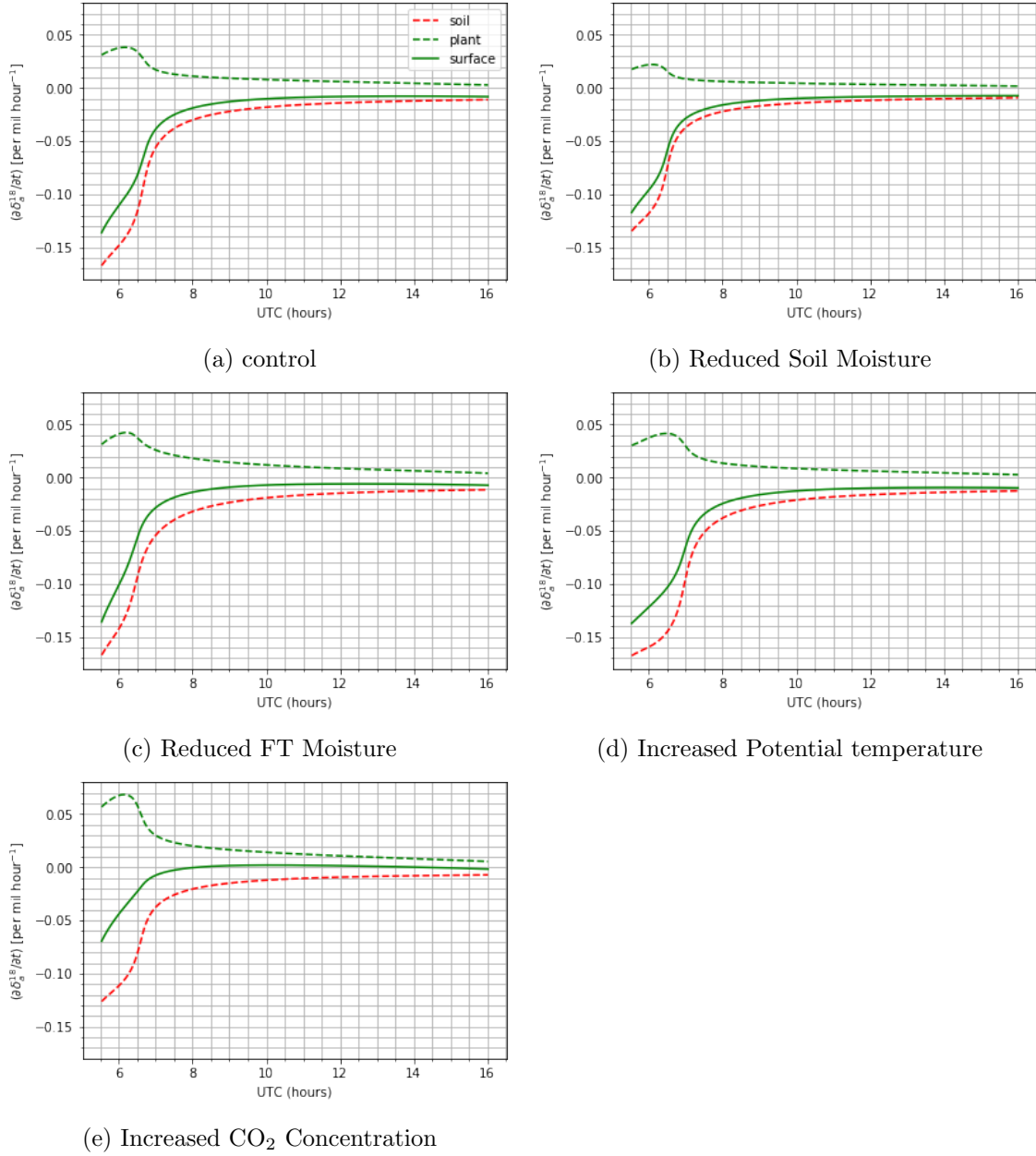(d) Increase Potential Temperature

(e) Increased CO$_2$ Concentration
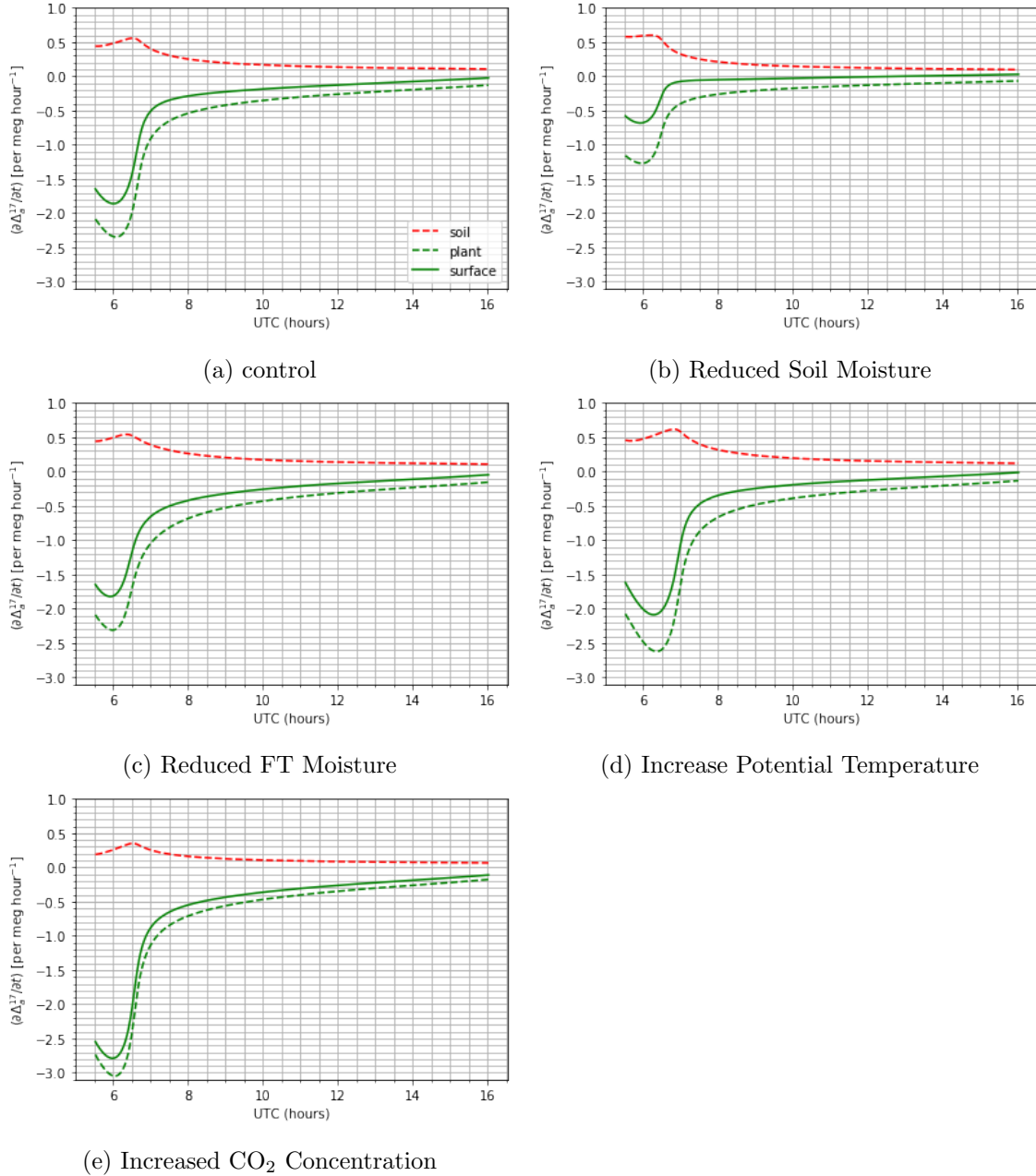
Figure B.2: Diurnal evolution of the surface contributions to the budget of $\Delta^{17}O(CO_2)$ for the different sensitivity analyses: a) control case, b) decrease in soil moisture, c) decreased moisture in the free troposphere, d) increase in the initial potential temperature of the ABL, and e) increase in the CO$_2$ concentration in the ABL. The different contributions to the $\Delta^{17}O$ budget are highlighted in the legend in B.2a.

Bibliography

Abe, O. (2008), 'Isotope Fractionation of Molecular Oxygen during Adsorption/Desorption by Molecular Sieve Zeolite', *Rapid Communications in Mass Spectrometry* **22**, 2510–2514.

Adnew, G. A., Hofmann, M. E., Paul, D., Laskar, A., Surma, J., Albrecht, N., Pack, A., Schwieters, J., Koren, G., Peters, W. & Röckmann, T. (2019), 'Determination of the Triple Oxygen and Carbon Isotopic Composition of CO_2 from Atomic Ion Fragments formed in the Ion Source of the 253 Ultra High-Resolution Isotope Ratio Mass Spectrometer', *Rapid Communications in Mass Spectrometry* **33**, 1363–1380.

Arrhenius, S. (1889), 'Über die Dissociationswärme und den Einfluss der Temperatur auf den Dissociationsgrad der Elektrolyte', *Zeitschrift für Physikalische Chemie* **4U**.

Barkan, E. & Luz, B. (2012), 'High-Precision Measurements of $^{17}O/^{16}O$ and $^{18}O/^{16}O$ Ratios in CO_2', *Rapid Communications in Mass Spectrometry* .

Barkan, E., Musan, I. & Luz, B. (2015), 'High-Precision Measurements of $\delta^{17}O$ and 17O Excess of NBS19 and NBS18', *Rapid Communications in Mass Spectrometry* **29**, 2219–2224.

Brenninkmeijer, C., Kraft, P. & Mook, W. (1983), 'Oxygen Isotope Fractionation between CO_2 and H_2O', *Chemical Geology* **41**, 181–190.

Ciais, P., Denning, A. S., Tans, P. P., Berry, J. A., Randall, D. A., Collatz, G. J., Sellers, P. J., White, J. W. C., Trolier, M., Meijer, H. A. J. & et al. (1997), 'A Three-dimensional Synthesis Study of $\delta^{18}O$ in Atmospheric CO_2: 1. Surface Fluxes', *Journal of Geophysical Research: Atmospheres* **102**(D5), 5857–5872.

Craig, H. & Gordon, L. I. (1965), *Deuterium and Oxygen 18 Variations in the Ocean and the Marine Atmosphere*, Laboratorio di geologia nucleare.

Cuntz, M. (2003), 'A Comprehensive Global Three-Dimensional Model of $\delta^{18}O$ in Atmospheric CO_2: 1. Validation of Surface Processes', *Journal of Geophysical Research* **108**.

Eiler, J. M. & Schauble, E. (2004), '$^{18}O^{13}C^{16}O$ in Earth's Atmosphere', *Geochimica et Cosmochimica Acta* **68**, 4767–4777.

Farquhar, G. D., Lloyd, J., Taylor, J. A., Flanagan, L. B., Syvertsen, J. P., Hubick, K. T., Wong, S. C. & Ehleringer, J. R. (1993), 'Vegetation Effects on the Isotope Composition of Oxygen in Atmospheric CO_2', *Nature* **363**, 439–443.

Francey, R. J. & Tans, P. P. (1987), 'Latitudinal Variation in Oxygen-18 of Atmospheric CO_2', *Nature* **327**(6122), 495–497.

Gillon, J. & Yarik, D. (2001), 'Influence of Carbonic Anhydrase Activity in Terrestrial Vegetation on the ^{18}O Content of Atmospheric CO_2', *Science* **291**(5513), 2584–2587.

Griffis, T. J., Sargent, S. D., Baker, J. M., Lee, X., Tanner, B. D., Greene, J., Swiatek, E. & Billmark, K. (2008), 'Direct Measurement of Biosphere-Atmosphere Isotopic CO_2 Exchange using the Eddy Covariance Technique', *Journal of Geophysical Research* **113**(D8).

Hoag, K. J., Still, C. J., Fung, I. Y. & Boering, K. A. (2005), 'Triple Oxygen Isotope Composition of Tropospheric Carbon Dioxide as a Tracer of Terrestrial Gross Carbon Fluxes', *Geophysical Research Letters* **32**.

Hofmann, M., Horváth, B., Schneider, L., Peters, W., Schützenmeister, K. & Pack, A. (2017), 'Atmospheric Measurements of $\delta^{17}O$ in CO_2 in Göttingen, Germany Reveal a Seasonal Cycle Driven by Biospheric Uptake', *Geochimica et Cosmochimica Acta* **199**, 143–163.

Janssen, C. (2020), 'Calculation of CO_2-O_2 Fractionation Factors'. French National Centre for Scientific Research, personal communication.

Joiner, J., Yoshida, Y., Zhang, Y., Duveiller, G., Jung, M., Lyapustin, A., Wang, Y. & Tucker, C. (2018), 'Estimation of Terrestrial Global Gross Primary Production (GPP) with Satellite Data-Driven Models and Eddy Covariance Flux Data', *Remote Sensing* **10**(9), 1346.

Kapiluto, Y., Yakir, D., Tans, P. & Berkowitz, B. (2007), 'Experimental and Numerical Studies of the ^{18}O Exchange Between CO_2 and Water in the Atmosphere–Soil Invasion Flux', *Geochimica et Cosmochimica Acta* **71**(11), 2657–2671.

Koren, G. (2020), Exchange of CO_2 between the Biosphere and Atmosphere in the Amazon Region, PhD thesis, chapter 3, PhD thesis.

Koren, G., Schneider, L., van der Velde, I. R., van Schaik, E., Gromov, S. S., Adnew, G. A., Mrozek Martino, D. J., Hofmann, M. E. G., Liang, M.-C., Mahata, S., Bergamaschi, P.,

van der Laan-Luijkx, I. T., Krol, M. C., Röckmann, T. & Peters, W. (2019), 'Global 3-D Simulations of the Triple Oxygen Isotope Signature 17O in Atmospheric CO_2', *Journal of Geophysical Research: Atmospheres* **124**.

Kruijt, B., Witte, J.-P. M., Jacobs, C. M. & Kroon, T. (2008), 'Effects of Rising Atmospheric CO_2 on Evapotranspiration and Soil Moisture: A Practical Approach for the Netherlands', *Journal of Hydrology* **349**(3-4), 257–267.

Landais, A., Barkan, E., Yakir, D. & Luz, B. (2006), 'The Triple Isotopic Composition of Oxygen in Leaf Water', *Geochimica et Cosmochimica Acta* **70**, 4105–4115.

Lee, X., Griffis, T. J., Baker, J. M., Billmark, K. A., Kim, K. & Welp, L. R. (2009), 'Canopy-scale Kinetic Fractionation of Atmospheric Carbon Dioxide and Water Vapor Isotopes', *Global Biogeochemical Cycles* **23**(1).

Mahata, S., Bhattacharya, S. K., Wang, C.-H. & Liang, M.-C. (2013), 'Oxygen Isotope Exchange between O_2 and CO_2 over Hot Platinum: An Innovative Technique for Measuring 17O in CO_2', *Analytical Chemistry* **85**, 6894–6901.

Meijer, H. & Li, W. (1998), 'The use of electrolysis for accurate delta O-17 and delta O-18 isotope measurements in water', *Isotopes in Environmental and Health Studies* **34**(4), 349–369.

Miller, J. B., Yakir, D., White, J. W. C. & Tans, P. P. (1999), 'Measurement of $^{18}O/^{16}O$ in the Soil-Atmosphere CO_2 Flux', *Global Biogeochemical Cycles* **13**(761–774).

Noilhan, J. & Mahfouf, J.-F. (1996), 'The ISBA Land Surface Parameterisation Scheme', *Global and Planetary Change* **13**(1-4), 145–159.

Richet, P., Bottinga, Y. & Javoy, M. (1977), 'A Review of Hydrogen, Carbon, Nitrogen, Oxygen, Sulphur, and Chlorine Stable Isotope Fractionation Among Gaseous Molecules', *Annual Review of Earth and Planetary Sciences* **5**, 65–110.

Super, I., Arellano, J. V.-G. D. & Krol, M. C. (2015), 'Cumulative Ozone Effect on Canopy Stomatal Resistance and the Impact on Boundary Layer Dynamics and CO_2 Assimilation at the Diurnal Scale: A Case Study for Grassland in the Netherlands', *Journal of Geophysical Research: Biogeosciences* **120**(7), 1348–1365.

Tans, P. P. (1998), 'Oxygen Isotopic Equilibrium Between Carbon Dioxide and Water in Soils', *Tellus B* **50**(2), 163–178.

Thiemens, M. H. (2006), 'History and Applications of Mass-Independent Isotope Effects', *Annual Review of Earth and Planetary Sciences* **34**, 217–262.

van Heerwaarden, C. C. V., Vilà-Guerau de Arellano, J., Moene, A. F. & Holtslag, A. A. M. (2009), 'Interactions Between Dry-Air Entrainment, Surface Evaporation and Convective Boundary-Layer Development', *Quarterly Journal of the Royal Meteorological Society* **135**(642), 1277–1291.

Vilà-Guerau de Arellano, J., Koren, G., Ouwersloot, H. G., Velde, I. V. D., Röckmann, T. & Miller, J. B. (2019), 'Sub-diurnal Variability of the Carbon Dioxide and Water Vapor Isotopologues at the Field Observational Scale', *Agricultural and Forest Meteorology* **275**, 114–135.

Vilà-Guerau de Arellano, J. & van Heerwaarden, C. C. (2015), *Atmospheric Boundary Layer: Integrating Air Chemistry and Land Interactions*, Cambridge University Press.

Wingate, L., Ogée, J., Cuntz, M., Genty, B., Reiter, I., Seibt, U., Yakir, D., Maseyk, K., Pendall, E. G., Barbour, M. M. & et al. (2009), 'The Impact of Soil Microorganisms on the Global Budget of $\delta^{18}O$ in Atmospheric CO_2', *Proceedings of the National Academy of Sciences* **106**(52), 22411–22415.

Yung, Y. L., DeMore, W. B. & Pinto, J. P. (1991), 'Isotopic Exchange Between Carbon Dioxide and Ozone via O(1D) in the Stratosphere', *Geophysical Research Letters* **18**, 13–16.